

Ice aggregation in Arctic shallow mixed-phase clouds: enhanced by dendritic growth and absent close to the melting level

Giovanni Chellini¹, Rosa Gierens¹, and Stefan Kneifel¹

¹University of Cologne

November 22, 2022

Abstract

Shallow mixed-phase clouds (MPCs) occur extensively in the Arctic, and are known to play a key role for the energy budget. While their characteristic structure is nowadays well understood, the significance of different precipitation-formation processes, such as aggregation and riming, is still unclear. Using a 3-year dataset of vertically-pointing W-band cloud radar and K-band Micro Rain Radar (MRR) observations from Ny-Ålesund, Svalbard, we statistically assess the relevance of aggregation in Arctic low-level MPCs. Combining radar observations with thermodynamic profiling, we find that larger snowflakes (mass median diameter above 1 mm) are predominantly produced in shallow MPCs whose mixed-phase layer is at temperatures between -15 and -10°C. This coincides with the temperature regime known for favoring aggregation due to growth and subsequent mechanical entanglement of dendritic crystals. Doppler velocity information confirms that these signatures are likely due to enhanced ice particle growth by aggregation. Signatures indicative of enhanced aggregation are however not distributed uniformly across the cloud deck, and only observed in limited regions, suggesting a link with dynamical effects. Low Doppler velocity values further indicate that significant riming of large particles is unlikely at temperatures below -5°C. Surprisingly, we find no evidence of enhanced aggregation at temperatures above -5°C, as is typically observed in deeper cloud systems. Possible reasons are discussed, likely connected to the ice habits that form above -10°C, increased riming, and lack of already aggregated particles precipitating from higher altitudes.

1 **Ice aggregation in Arctic shallow mixed-phase clouds:**
2 **enhanced by dendritic growth and absent close to the**
3 **melting level**

4 **G. Chellini¹, R. Gierens¹, and S. Kneifel¹**

5 ¹Institute for Geophysics and Meteorology, University of Cologne, Cologne, Germany

6 **Key Points:**

- 7 • Arctic shallow MPCs produce large ice aggregates predominantly at dendritic-growth
8 temperatures
9 • The typically observed enhanced aggregation zone close to 0°C is absent in Arc-
10 tic shallow MPCs
11 • Enhanced aggregation due to dendritic growth occurs intermittently in limited re-
12 gions of the MPC

Corresponding author: Giovanni Chellini, g.chellini@uni-koeln.de

Abstract

Shallow mixed-phase clouds (MPCs) occur extensively in the Arctic, and are known to play a key role for the energy budget. While their characteristic structure is nowadays well understood, the significance of different precipitation-formation processes, such as aggregation and riming, is still unclear.

Using a 3-year dataset of vertically-pointing W-band cloud radar and K-band Micro Rain Radar (MRR) observations from Ny-Ålesund, Svalbard, we statistically assess the relevance of aggregation in Arctic low-level MPCs. Combining radar observations with thermodynamic profiling, we find that larger snowflakes (mass median diameter above 1 mm) are predominantly produced in shallow MPCs whose mixed-phase layer is at temperatures between -15 and -10°C . This coincides with the temperature regime known for favoring aggregation due to growth and subsequent mechanical entanglement of dendritic crystals. Doppler velocity information confirms that these signatures are likely due to enhanced ice particle growth by aggregation. Signatures indicative of enhanced aggregation are however not distributed uniformly across the cloud deck, and only observed in limited regions, suggesting a link with dynamical effects. Low Doppler velocity values further indicate that significant riming of large particles is unlikely at temperatures below -5°C .

Surprisingly, we find no evidence of enhanced aggregation at temperatures above -5°C , as is typically observed in deeper cloud systems. Possible reasons are discussed, likely connected to the ice habits that form above -10°C , increased riming, and lack of already aggregated particles precipitating from higher altitudes.

Plain Language Summary

Shallow mixed-phase clouds (MPCs), i.e. shallow clouds containing both liquid droplets and ice crystals, form frequently in the Arctic region. Their characteristic structure -consisting of one or multiple liquid layers at sub-zero temperatures, from which ice crystals form and precipitate- is nowadays well understood. However, the processes that lead to the growth of ice crystals into snow have been overlooked.

Using a 3-year dataset of radar observations from Ny-Ålesund, in Svalbard, Norway, we are able to identify situations when the ice particle growth is dominated by aggregation of several individual crystals. Combining radar observations with temperature information, we find that larger snowflakes are only produced in MPCs if their liquid portion is at temperatures between -15 and -10°C . This coincides with the temperature regime known for favoring aggregation due to growth and subsequent entanglement of branched crystals.

Surprisingly, we find no evidence of enhanced ice aggregation at temperatures above -5°C , as is typically observed in deeper cloud systems. Possible reasons are discussed, likely connected to the ice crystal shapes that develop above -10°C , increased liquid droplet production, and lack of already aggregated particles precipitating from higher altitudes.

1 Introduction

Shallow mixed-phase clouds (MPCs) are ubiquitous in the Arctic. They have been shown to occur widely and frequently (e.g., Morrison et al., 2012; Mioche et al., 2015) and to persist typically for several hours (de Boer et al., 2009; Shupe, 2011), with some recorded cases lasting up to several days (e.g., Zuidema et al., 2005). They are further known to introduce, on average, a strong positive surface radiative forcing (Shupe & Intrieri, 2004; Serreze & Barry, 2011; Matus & L'Ecuyer, 2017; Tan & Storelvmo, 2019). Arctic shallow MPCs display a characteristic structure with one or multiple shallow liquid layers close to cloud top, from which ice particles form and precipitate (Shupe et al.,

2006b). Their persistence is due to a complex interplay of several processes (Morrison et al., 2012), and they have been found to occur under a variety of conditions, including both stable and unstable stratification, and under a wide spectrum of aerosol concentrations (Jackson et al., 2012; Sotiropoulou et al., 2014; Kalesse, de Boer, et al., 2016; Young et al., 2016; Gierens et al., 2020). Intense cloud-top radiative cooling caused by the supercooled liquid close to cloud top drives buoyant production of turbulence in the cloud layer, which, in turn, drives condensation and maintains the liquid layer (Solomon et al., 2011).

The frequent formation of precipitation in Arctic mixed-phase clouds has been demonstrated by several studies, as far back as Rangno and Hobbs (2001) and Harrington and Olsson (2001). More recently, Silber, Fridlind, et al. (2021) observed that more than 85% of clouds containing supercooled liquid above Utqiagvik, Alaska, precipitate continuously. Precipitation from MPCs, especially when deposited to the surface, withdraws moisture and ice nuclei from the MPC (Morrison et al., 2012; Solomon et al., 2014, 2015). Lower cloud fractions and faster dissipation have been suggested for Arctic stratocumuli that develop precipitation (Harrington & Olsson, 2001; Simpfendorfer et al., 2019). It can then be expected that in addition to cloud lifetime, precipitation further affects the phase and radiative characteristics of the MPC (Harrington & Olsson, 2001; Avramov & Harrington, 2010; Solomon et al., 2015; Tan & Storelvmo, 2019; Eirund et al., 2019; Proske et al., 2021). Tan and Storelvmo (2019) have shown that in the Community Earth System Model (CESM) Arctic amplification increases the larger the ice particles in Arctic MPCs are, because of a stronger cloud-phase feedback. Furthermore, Proske et al. (2021) argue that, out of all microphysical processes, aggregation is the dominant mechanism affecting ice water path and cloud radiative effects, and therefore has the largest need to be represented correctly in climate models. Gaining process-level understanding of precipitation formation in Arctic shallow MPCs is thus necessary for an accurate representation of these clouds. In particular, the role of individual ice-growth processes, such as aggregation and riming, in the formation of precipitation in Arctic low-level MPCs is still unclear.

In-situ observations of ice particles in Arctic shallow MPCs reported in literature vary largely: pristine ice crystals, aggregates, and rimed particles have all been observed (McFarquhar et al., 2007; Avramov et al., 2011; Mioche et al., 2017; Wendisch et al., 2019). McFarquhar et al. (2007) reported observing mostly irregular and rimed branched crystals at cloud base, from in-situ aircraft observations at Utqiagvik, Alaska. At the same site Avramov et al. (2011) observed dendrites and large aggregates. Mioche et al. (2017) compiled in-situ observations from several aircraft campaigns above the Greenland and Norwegian seas, reporting large fractions of rimed or irregular ice particles. Fitch and Garrett (2022) reported, based on long-term ground-based in-situ observations, that, at Oliktok Point, Alaska, 65% of all frozen precipitation displays some degree of riming, even with observed liquid water path of less than 50 g/m².

In this study we investigate the significance of different ice-growth processes, with a focus on aggregation, for precipitation formation in Arctic MPCs, using a long-term dataset of vertically-pointing dual-frequency (K- and W-band) radar observations, from the high-Arctic site of Ny-Ålesund, Svalbard, Norway. Radar observations obtained at different wavelengths can be combined in order to derive mean particle size of the hydrometeor population based on their differential scattering properties (Battaglia et al., 2020). The dual-wavelength ratio (DWR), i.e. the ratio of equivalent radar reflectivity factors at two separate frequencies, increases when particles grow in size and transition from the Rayleigh scattering regime into the non-Rayleigh scattering regime (e.g., Hogan et al., 2000; Liao et al., 2005). When combined with in-cloud temperature and filtering for intense riming using vertical Doppler velocity information, DWR information has been used to derive the typical temperature regions favoring aggregation for mid-latitude clouds by e.g. Dias Neto et al. (2019) and Barrett et al. (2019). These authors observed a first

114 noticeable increase in DWR at Ka- and W-band to occur in the temperature interval from
 115 -15 to -10°C, consistently with early cloud chamber studies (e.g., Kobayashi, 1957). Said
 116 temperature region is part of the often-called dendritic-growth zone (DGZ), where sev-
 117 eral plate-like particle habits are preferentially growing, including dendrites. The DGZ
 118 extends from -20 to -10°C, with enhanced depositional growth between -18 and -12°C
 119 (Takahashi et al., 1991; Takahashi, 2014). The dendrites' large cross-sectional area and
 120 ability to mechanically entangle their branches favor a rapid formation of aggregates (Pruppacher
 121 & Klett, 2012; Connolly et al., 2012). A second enhanced aggregation zone close to 0°C
 122 is often observed as well, revealed by a further increase in DWRs at several frequency
 123 combinations (W-, Ka-, Ku-, and X-band) (Chase et al., 2018; Dias Neto et al., 2019;
 124 Tridon et al., 2019). Close to the melting level the presence of a quasi-liquid layer on the
 125 ice particles (Fletcher, 1962; Slater & Michaelides, 2019) is thought to favor intense ag-
 126 gregation (Fabry & Zawadzki, 1995).

127 Here, we obtain 3-year statistics of DWR in Arctic shallow MPCs, by combining
 128 radar observations from a W-band cloud radar and a K-band precipitation radar, the
 129 Micro Rain Radar 2 (MRR-2). We further combine radar observations with thermody-
 130 namic retrievals from a co-located microwave radiometer. This publication is thus struc-
 131 tured as follows: essential theoretical aspects of dual-wavelength radar observations are
 132 explained in section 2, the instruments and further techniques used are described in sec-
 133 tion 3, results are shown and discussed in section 4, and finally the main conclusions and
 134 questions raised by this study are summarized in section 5.

135 **2 Background: dual-wavelength radar approach**

136 The equivalent radar reflectivity factor Z_e (hereafter called reflectivity) for an en-
 137 semble of scatterers in the measurement volume is defined as:

$$Z_e = \frac{\lambda^4}{\pi^5} \|K_W\|^{-2} \int_0^\infty N(\sigma_b) \sigma_b(\lambda) d\sigma_b, \quad (1)$$

138 where λ is the transmitted signal wavelength, $\|K_W\|^2$ is the dielectric constant of liq-
 139 uid water, σ_b is the backscattering cross-section of the individual scatterers, and $N(\sigma_b)$
 140 the number distribution across the scatterer population (Fabry, 2018). Z_e thus depends
 141 on both size (through σ_b) and concentration of particles (through $N(\sigma_b)$), in addition
 142 to habit, phase, and orientation, and does not provide unequivocal information on par-
 143 ticle size. Following the definition of Z_e , values measured at two wavelengths are equal
 144 if scattering from all particles and at both wavelengths can be approximated by Rayleigh
 145 scattering. If the particles increase in size, they first start to deviate from Rayleigh scat-
 146 tering at the shorter wavelength: this leads to a smaller Z_e at the shorter wavelength
 147 compared to the longer one, where more particles are still in the Rayleigh scattering regime
 148 (Battaglia et al., 2020). As a result, quantities combining Z_e values at both wavelengths
 149 can be related to the characteristic size of the underlying particle size distribution (Hogan
 150 et al., 2000; Matrosov et al., 2005; Liao et al., 2005; Szyrmer & Zawadzki, 2014; Tridon
 151 & Battaglia, 2015; Kneifel et al., 2016).

152 The most commonly used variable to quantify differential scattering of the radar
 153 beams at two separate wavelengths is the Dual-Wavelength Ratio (DWR, sometimes named
 154 Dual-Frequency Ratio, DFR), defined as:

$$DWR_{\lambda_1, \lambda_2} = \frac{Z_{e, \lambda_1}}{Z_{e, \lambda_2}}, \quad (2)$$

155 where Z_{e, λ_i} are the equivalent reflectivity factors in linear units and λ_1 is commonly cho-
 156 sen to be larger than λ_2 . With this convention $DWR = 0$ dB if particles scatter accord-
 157 ing to the Rayleigh regime at both wavelengths and if their $\|K_W\|^2$ (Eq. 1) are identi-
 158 cal or have been corrected for. DWR values increase as particles transition into non-Rayleigh

159 scattering at the shorter wavelength, then reach a saturation value as non-Rayleigh scat-
 160 tering is reached at both wavelengths. As a result, the DWR can be used as a proxy for
 161 the mean size of the sampled particle population (Hogan et al., 2000; Liao et al., 2005;
 162 Kneifel et al., 2016). The relation between DWR and particle size is, however, not uni-
 163 vocal, and further depends on the particle shape and density (e.g., Matrosov et al., 2019)
 164 as well as on the particle size distribution (PSD) shape (Mason et al., 2019). Using the
 165 scattering database of Ori et al. (2021) and dendrite aggregates as well as a simple in-
 166 verse exponential PSD, we find for example a DWR_{K-W} of 3 (6, 9) dB to correspond
 167 to a mass median diameter of 1.5 (2.4, 3.7) μm , respectively. The maximum DWR value
 168 for such modeled dendrite aggregates is 11.4 dB, obtained for a mass median diameter
 169 of 8.1 μm , while the saturation DWR value is 9.4 dB. The full dependency of DWR on
 170 mass median diameter for different particle types is shown in Appendix A.

171 3 Datasets and methods

172 3.1 Measurement site

173 The observations analyzed in this study were carried out at the observatory of the
 174 Arctic research base AWIPEV in Ny-Ålesund, Svalbard. Ny-Ålesund is located at 79°N,
 175 in the region where Arctic amplification is the most intense (e.g., Dahlke & Maturilli,
 176 2017). The site is located 13 m above sea level close to the coast of the Kongsfjorden,
 177 a fjord with surrounding mountains with altitudes of 500 to 1000 m. Similar to other
 178 locations in the Arctic, the lower troposphere above Ny-Ålesund is often stably strat-
 179 ified. Temperature and humidity inversions have been found in respectively 75 and 84%
 180 of the daily radiosondes launched between 1993 and 2014 (Maturilli & Kayser, 2017).
 181 Mean monthly values of surface air temperature have been observed to range between
 182 5.8°C in July and -12.0°C in March (Maturilli et al., 2013) and average yearly precip-
 183 itation has been measured to be 564 mm/year with a large standard deviation of 444 mm/year,
 184 in the 2012-2019 period (Mori et al., 2021). Furthermore, remote sensing observations
 185 of clouds at this location have already been analyzed in depth by previous studies, such
 186 as Nomokonova, Ebell, et al. (2019), Vassel et al. (2019), Nomokonova et al. (2020), Gierens
 187 et al. (2020), and Ebell et al. (2020).

188 While clouds in general occur at the site 60-80% of the time (Shupe, 2011; Maturilli
 189 & Ebell, 2018; Nomokonova, Ebell, et al., 2019), Nomokonova, Ebell, et al. (2019) ob-
 190 served a frequency of occurrence of 20.6% for single-layer MPCs (with no restriction on
 191 cloud depth or cloud-top height). They report an average LWP of 66 g/m^2 , and aver-
 192 age IWP of 164 g/m^2 for this cloud type. Gierens et al. (2020) estimated the occurrence
 193 of low-level MPCs lasting more than 1 hour to be 23%, with average LWP and IWP val-
 194 ues of 35 and 12 g/m^2 , respectively. Frequency of occurrence, LWP and IWP values from
 195 these two studies are similar to those observed during the Surface Heat Budget of the
 196 Arctic Ocean (SHEBA) campaign (Shupe et al., 2006a), at Iqaluit, Alaska (de Boer et
 197 al., 2009; Zhao & Wang, 2010), and at Eureka, Nunavut, Canada (de Boer et al., 2009).
 198 The height of the liquid base of low-level MPCs ranges typically between 0.54 to 1.0 km,
 199 which is at or above the height of the surrounding mountaintops (Gierens et al., 2020).

200 3.2 Radar systems

201 In this study, we calculate DWRs (K- and W-band) of MPCs based on continu-
 202 ous zenith-pointing radar observations available from September 2017 to October 2018,
 203 and from June 2019 to February 2021. The W-band observations are obtained with 94-
 204 GHz frequency-modulated continuous wave (FMCW) Doppler cloud radars (RPG-FMCW-
 205 94-SP, manufactured by Radiometer Physics GmbH (RPG); Küchler et al. (2017)). Ob-
 206 servations from two slightly different RPG-FMCW-94-SP radar systems have been com-
 207 bined: during the first time period, observations were collected with the MiRAC-A (Mech
 208 et al., 2019) which has a slightly larger beamwidth than the JOYRAD-94 (Küchler et

	JOYRAD-94	MiRAC-A	MRR-2
Central frequency	94.0 GHz	94.0 GHz	24.23 GHz
Time res.	2-3 s	2-3 s	60 s
Integration time	0.5-0.6 s	0.5-0.6 s	60 s
Range res.	4-5.3 m	3.2-7.5 m	30 m
Min. range	100 m	100 m	30 m
Max. range	12 km	12 km	960 m
Sensitivity at 100 m	-62 dBZ	-64 dBZ	-13 dBZ
Sensitivity at 900 m	-50 dBZ	-50 dBZ	-6 dBZ
Beam width (half power)	0.5°	0.85°	1.5°

Table 1. Selected technical specifications of the three radar systems used in this study: two cloud radars, JOYRAD-94 and MiRAC-A, and a precipitation radar, MRR-2. Further information on the instruments can be found, respectively, in K uchler et al. (2017), Mech et al. (2019), and Klugmann et al. (1996).

209 al., 2017) used from June 2019 onwards. Both systems collected data with a temporal
 210 resolution of 2-3 s and vertical resolutions between 3-8 m depending on the range region
 211 (for technical details of the radars see Table 1, K uchler et al. (2017), and Gierens (2021)).
 212 The measurements were set up with a minimum and maximum range of 100 m and 12
 213 km, respectively.

214 The W-band observations are complemented by observations from a K-band (24
 215 GHz), zenith-pointing, FMCW Doppler Micro Rain Radar (MRR-2, Metek GmbH; Klugmann
 216 et al. (1996)). Due to its economic and light-weight design it has been frequently used
 217 to study snowfall in mountainous (Cha et al., 2009; Kneifel et al., 2011) and polar re-
 218 gions (Grazioli et al., 2017; Dur an-Alarc on et al., 2019), evaluate satellite products (Maahn
 219 et al., 2014; Souverijns et al., 2018) and model performance (Scarchilli et al., 2020). We
 220 use the processing method developed by Maahn and Kollias (2012), which is fine-tuned
 221 for observations of frozen hydrometeors. The resolution in time (60 s) and range (30 m)
 222 is much coarser than the W-band cloud radars. Its average sensitivity for this measure-
 223 ment set up ranges between -13 and -6 dBZ, depending on range. Said sensitivity was
 224 calculated as the mean average noise level times 1.2, as that is the lowest threshold for
 225 spectral reflectivity values to be considered signal in the processing routine by Maahn
 226 and Kollias (2012).

227 In order to calculate DWRs, we averaged the W-band data to the MRR resolution.
 228 Note that during the study period the MRR was set up to measure with a maximum range
 229 of 960 m. Calculated DWRs are therefore only available from the lowest W-band range
 230 gate (100 m) up to this height. Mean Doppler Velocity (MDV) is taken from the W-band
 231 cloud radars.

232 **3.2.1 Radar calibration evaluation**

233 Since the aim of our analysis is gaining information on particle size based on DWR
 234 calculated from Z_e at K- and W-band, evaluating the calibration (especially in a rela-
 235 tive sense) of all radar systems involved is necessary. The radar calibration constant might
 236 change, e.g. due to drifts, which can lead to biases in the measured Z_e . In our analy-

MRR-2 yearly JJAS offsets (dB)	-0.81, -1.33, -1.57, -1.88, -1.91
MiRAC-A monthly offsets (dB)	2.75, 3.25, 3.75, 2.25, 4.75, 2.25, 2.75, 2.75, 1.25, 0.75, 0.75, 1.25, 2.75
JOYRAD-94 monthly offsets (dB)	1.75, -0.25, -0.25, -0.25, 0.75, 1.25, 2.25, 2.25, 1.75, 0.75, 0.75, 5.25, 0.25, -0.25, -0.25, 1.25, -0.25, 3.25, 1.75, 1.25, 1.25

Table 2. Calibration offsets obtained for the three radar systems used in the study. The offsets indicated for the MRR-2 were obtained yearly for the period from June to September. Monthly offsets for the remaining months were obtained by linear interpolation of the indicated values. Offsets indicated for JOYRAD-94 and MiRAC-A were calculated monthly. Offsets are reported in chronological order.

237 sis, we obtained calibration offsets for the MRR following a widely used disdrometer-based
 238 approach (e.g., Dias Neto et al., 2019; Myagkov et al., 2020). The W-band radars were
 239 instead calibrated using a DWR-based approach, requiring that the DWR distribution
 240 has its mode at 0 dB. All the derived offsets are reported in Table 2.

241 At the AWIPEV site a Parsivel disdrometer (Löffler-Mang & Joss, 2000) is installed,
 242 and data are available for the whole study period. Parsivel measures volume-equivalent
 243 sizes and fall speeds of particles that fall through its laser beam. It thus provides par-
 244 ticle size distributions, and fall speed distributions for the particle population. A crit-
 245 ical assessment of its performance can be found in Battaglia et al. (2010). The disdrometer-
 246 based calibration method consists in forward simulating Z_e values from drop size dis-
 247 tribution observed by Parsivel during rain events. The simulated reflectivities were then
 248 compared with the observed ones, taken from the range gate between 120 and 150 m.
 249 We selected the rain events based on the following criteria:

- 250 • Disdrometer detects liquid precipitation. If frozen precipitation is detected all liq-
 251 uid within 10 minutes is ignored.
- 252 • Only data from June through September are used, and only when surface tem-
 253 perature (from nearby weather station) is greater than 5°C, in order to exclude
 254 misclassified frozen or partially melted precipitation.
- 255 • Disdrometer data are only used if rain rate ≥ 0.1 mm/h following the approach
 256 by Williams et al. (2005). Additionally only measurements containing at least 25
 257 samples per minute are used. Both criteria are required in order for the disdrom-
 258 eter measurements to be representative of the drop population.
- 259 • Drop size distributions (DSDs) from Parsivel must contain particles larger than
 260 1 mm. This criterion was determined following Myagkov et al. (2020), so that evap-
 261 oration of the drops between the chosen range gate and the ground doesn't affect
 262 the forward simulated Z_e values.
- 263 • Events are required to last at least one hour, with gaps allowed for a total of one
 264 sixth of the duration of the event.

265 Reflectivity values were based on the observed DSDs, and forward simulated with the
 266 T-matrix method (Waterman, 1965; Leinonen, 2014), using a drop shape model from Thurai
 267 et al. (2007). Following Huang et al. (2008), the drops were assumed to have Gaussian
 268 distributed canting angles, with 0° mean value and a 10° standard deviation. Attenu-
 269 ation due to liquid was simulated as well, and was subtracted from the forward simu-
 270 lated reflectivity values. All Z_e values below -10 dBZ and above 25 dBZ were excluded.
 271 It should be noted that we did not compare time series of observed and simulated Z_e but

rather compared the Z_e distribution of the total rainfall event. This mitigates the issue of time delays between Z_e observed at the lowest radar range gate and the surface observations. A single median reflectivity value was then obtained for all events in each June-through-September period, for both the observations and the forward simulation. In each period the Z_e offset was obtained by subtracting the two median values. In the periods from October to May, monthly Z_e offset values were calculated by linearly interpolating the obtained values. In the months from October 2020 to February 2021 the same offset obtained during the June-through-September period in 2020 was used.

We attempted to apply the same disdrometer-based approach to the calibration of the W-band radars, but we observed a strong dependence of the calculated offset values on the accumulated precipitation during the events. We hypothesize that this is due to deterioration of the coating of the radomes, leading to some of the rain water being absorbed by the radome, thus causing increasing attenuation of the signal. Although this phenomenon is not an issue for snowfall observations, it hampers the applicability of the disdrometer-based method to the W-band radars. For the MRR, we did not observe any attenuating effect due to wet antenna. Unlike the W-band radar, the MRR is not covered by a radome. Due to this reason we used the MRR as our reference and estimated the offsets of the W-band radars using a DWR-based approach in light snowfall. Although the MRR is quite limited in its maximum range, this approach using light snowfall is overall similar to relative calibration methods applied to cloud radars in low-reflectivity ice clouds (Dias Neto et al., 2019; Tridon et al., 2020). The relative offset estimated with this approach uses the fact that, for observations of Rayleigh-scattering frozen hydrometeors only, the DWR distribution has its mode at 0 dB. The radar measurements used for this calibration were selected with the following criteria:

- Signal corresponds to ice-only clouds, based on the Cloudnet target classification (see section 3.3).
- Z_e from MRR is between -5 and 0 dBZ, to ensure the presence of mostly Rayleigh scatterers in the radar volume.
- If Parsivel detects liquid precipitation, all echoes within 10 minutes are ignored.

Monthly DWR distributions for observations satisfying these conditions were then obtained, and the mode of the distribution was taken as monthly Z_e offset. The bins used to calculate the distributions are 0.5 dB wide. We estimated the uncertainty associated with this calibration approach by taking the left standard deviation of the monthly DWR distributions with respect to the mode. The root mean square value of such monthly uncertainties is 2.1 dB.

3.3 Temperature soundings and hydrometeor classification

Many microphysical processes are known to be strongly dependent on temperature (e.g., Pruppacher & Klett, 2012), we thus investigate the dependence of DWR statistics on in-cloud temperature, as well as cloud-top and cloud-base temperature. Additional information on cloud phase is also needed, to properly identify MPC events. For these reasons we use temperature profiles retrieved from a HATPRO (Humidity And Temperature PROfiler; Rose et al. (2005), Nomokonova, Ritter, and Ebell (2019)) microwave radiometer, and the Cloudnet target classification product (Hogan & O'Connor, 2004; Illingworth et al., 2007). The HATPRO is operated by the Alfred Wegener Institute (AWI) and measures on the same platform as the radar systems. In addition to temperature soundings, HATPRO observations are also used to retrieve liquid water path (LWP). In order to increase the accuracy of temperature profiles especially in the lowest 1 km, the observations at seven channels along the 60 GHz oxygen absorption band are obtained at various elevation angles (Crewell & Lohnert, 2007). In this way, the uncertainty (root mean square error) in temperature even in the presence of temperature inversions reaches a maximum value of 2 K (Gierens et al., 2020). Elevation scans are regularly performed

323 every 15 to 20 minutes. The profiles are linearly interpolated in time to the same res-
 324 olution as the MRR (60 s).

325 Observations from the W-band cloud radar, HATPRO, and a ceilometer (model
 326 Vaisala CL51; Maturilli and Ebell (2018)), together with output from the ICOSahedral
 327 Nonhydrostatic weather model (ICON; Zängl et al. (2015)), in its global numerical weather
 328 prediction mode (ICON-IGLO), are operationally combined into the Cloudnet product
 329 (Hogan & O’Connor, 2004; Illingworth et al., 2007). In particular, we use the target clas-
 330 sification product which classifies hydrometeors into: cloud droplets, supercooled cloud
 331 droplets and cloud ice, as well as drizzle or rain. The presence of liquid at sub-zero tem-
 332 peratures is mainly based on ceilometer observations. The ceilometer signal undergoes
 333 far greater attenuation when traversing a liquid layer, compared to an ice layer. This leads
 334 to limitations of the Cloudnet product if more than one liquid layer is present, as often
 335 the signal is unable to penetrate the lowest liquid layer. We will henceforth use the term
 336 *liquid base* to refer to the base of the lowest liquid layer detected by the ceilometer. We
 337 will further refer to the portion of the MPC above the liquid base as *mixed-phase layer*
 338 (MPL). In this study we use the Cloudnet target classification product to derive the height
 339 of the liquid base, and cloud-top height.

340 3.4 Selection of mixed-phase cloud events

341 Low-level MPC events were identified following an approach similar to that em-
 342 ployed by Gierens et al. (2020). Cloudnet data were first checked for the presence of shal-
 343 low ice- and liquid-containing clouds, meaning clouds with cloud top below 2500 m, and
 344 liquid and ice present at any height below 2500 m. Multiple cloud layers are considered
 345 as one if separated by 60 m or less, otherwise only the lowest layer is included in the anal-
 346 ysis, and the remaining ones are excluded.

347 During intense precipitation events snow might accumulate on the ceilometer aper-
 348 ture, thus leading to ceilometer data not being available, and liquid layers not being iden-
 349 tified in the Cloudnet target classification. When the ceilometer signal is not available,
 350 the presence of liquid is evaluated using the LWP retrievals from HATPRO. In these con-
 351 ditions clouds classified as ice only were also considered mixed-phase when LWP exceeded
 352 a threshold of 10 g/m². In parts of the analysis DWR at liquid base, and its maximum
 353 value below the liquid base are evaluated in each sample. When evaluating this quan-
 354 tity, only the subset of data where the ceilometer signal is available and the liquid base
 355 is within the MRR range was used.

356 MPC-events were then identified by requiring that liquid and ice were present for
 357 at least 60 minutes, with gaps allowed for a total of one sixth the total duration of the
 358 event. Using this method, we identified a total of 1605 shallow MPC cases, adding up
 359 to a total duration of 7592 hours. Out of these, 1042 cases, or 6022 hours, are above MRR
 360 sensitivity. Out of all cases (cases detected by the MRR), 23.6 % (25.6 %) were detected
 361 in winter, 15.4 % (18.0 %) in spring, 30.2 % (23.0 %) in summer, and 30.8 % (33.4 %) in
 362 autumn. In part of the analysis we only focus on MPC events detected by the MRR,
 363 and with surface temperature below 0°C: 508 cases satisfy these conditions.

364 4 Results and discussion

365 A typical shallow MPC event observed from 4 to 6 February 2021 is displayed in
 366 Fig. 1. The four panels depict Z_e and MDV from the W-band cloud radar, DWR, and
 367 LWP. The figure also shows the height of the liquid base and temperature contours, de-
 368 rived from the ceilometer and HATPRO, respectively. The event depicted in the figure
 369 produced precipitation characterized by a wide range of DWR values. In particular, the
 370 MPC produced high-DWR showers intermittently throughout its duration, highlighting
 371 the presence of large ice particles. These high-DWR showers are alternating with regions

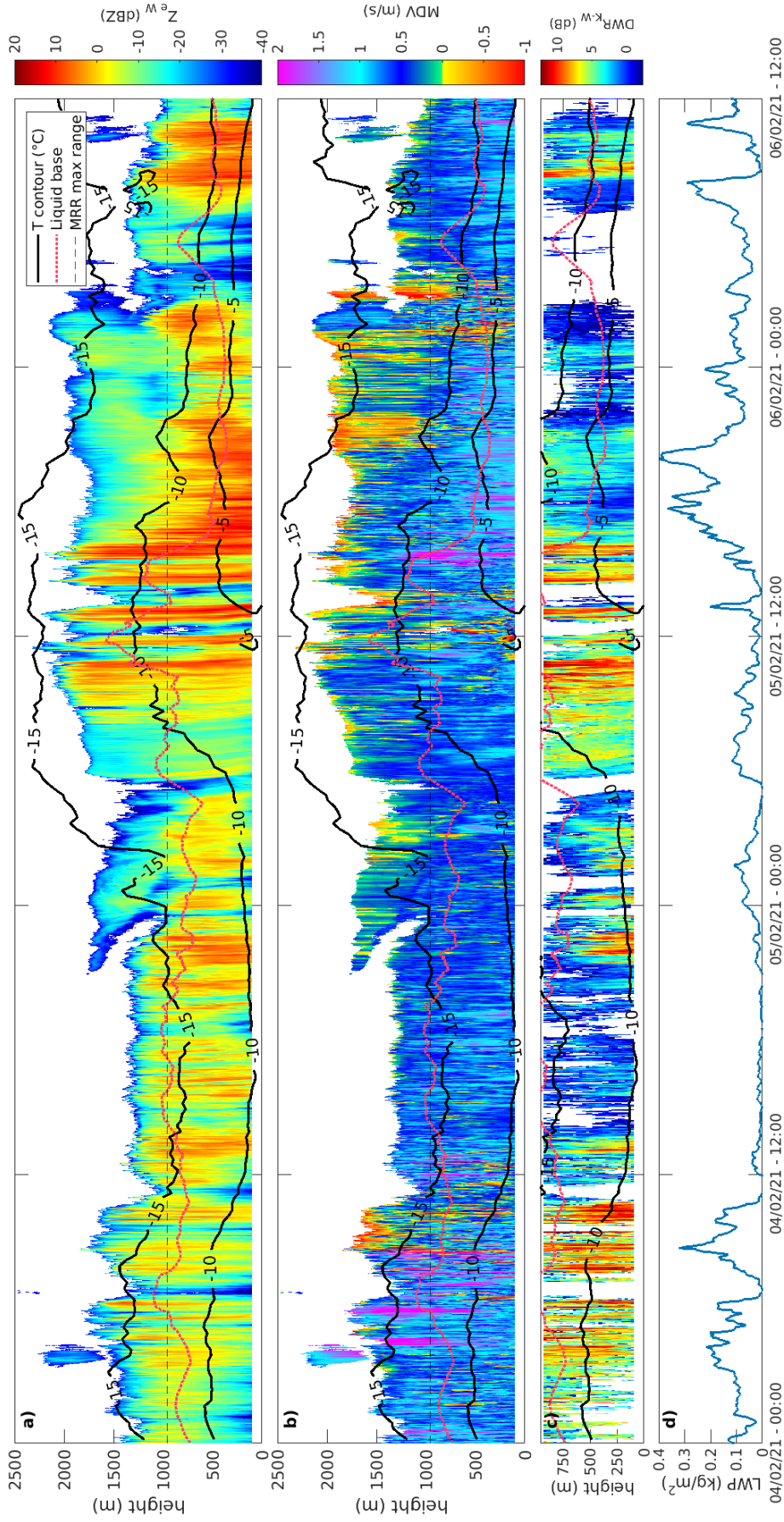


Figure 1. Example of shallow mixed-phase cloud event observed in Ny-Ålesund on 4 to 6 February 2021. Panels a and b display the reflectivity and mean Doppler velocity measured by the W-band cloud radar, respectively. Panel c depicts the Dual-Wavelength Ratio obtained from MRR and cloud radar observations. Panel d displays the LWP, retrieved from HATPRO microwave radiometer observations. In panels a, b, and c, contour lines indicate temperature (black) based on retrievals from HATPRO, and the liquid base height (pink dotted) from the Cloudnet target classification product. The horizontal dashed line in panels a and b indicates the maximum range of the MRR. Times indicated are in UTC.

372 characterized by lower DWR values, and even periods when the reflectivity was below
 373 the sensitivity of the MRR, and thus DWR values were not available. Fig. 1 shows that
 374 most high-DWR showers originate from within the mixed-phase layer. Interestingly, high
 375 DWR values are not necessarily linked to high reflectivity values, and vice versa.

376 **4.1 Impact of MRR sensitivity and limited maximum range on detected**
 377 **cloud characteristics**

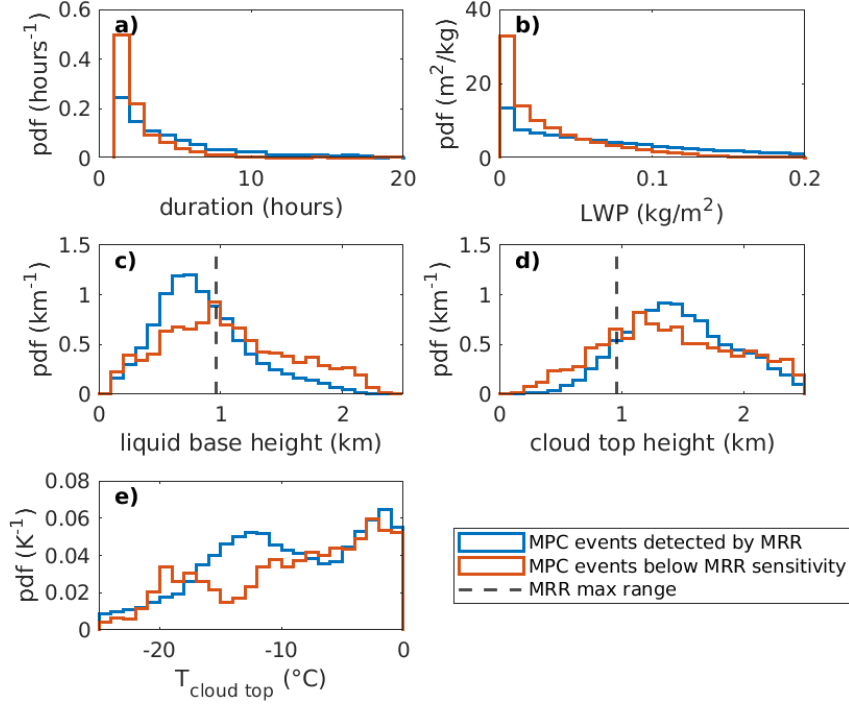


Figure 2. Statistics of mixed-phase cloud characteristics in Ny-Ålesund. Probability density functions (pdfs) are shown for events detected by the MRR, and for events that produced a reflectivity below the sensitivity of the MRR, and thus were only detected by the W-band cloud radar. The parameters shown are MPC event duration (a), liquid water path (LWP; b), liquid-base height (c), cloud-top height (d), and cloud-top temperature (e). The dashed lines in panels c and d indicate the maximum range of the MRR. Bin sizes are respectively: 1 h, 10 g m⁻², 100 m, 1°C.

378 In the following analysis we will focus only on MPC events detected by the MRR.
 379 The two limitations of the MRR are its maximum range (960 m), and lower sensitivity
 380 compared to the W-band cloud radars. To evaluate the effect of these limitations on the
 381 data sampled for the analysis, characteristics of MPCs detected by the MRR, and MPCs
 382 detected only by the W-band cloud radar are shown and compared in Fig. 2. Overall,
 383 MPCs detected by the MRR tend to last longer (median 4.0 hours) and display slightly
 384 higher LWP values (median 69.1 g/m²) compared to all MPC events (2.9 hours and 55.5
 385 g/m² respectively). Fig. 2e shows that the fraction of MPCs detected by the MRR
 386 with cloud-top temperatures between -20 and -10°C (84.8%) is higher than that for MPCs
 387 with cloud-top temperatures above -10°C (75.6%). Moreover the number of MPC events
 388 with cloud-top T below -20°C is very low (93), and most of these clouds are detected by
 389 the MRR (81.5%). While 66.2 % of MPCs detected by the MRR have their liquid base
 390 within the instrument’s maximum range, only 12.4% have their top within it (Fig. 2c,

391 d). For this reason the analysis reported in the following sections focuses on precipita-
 392 tion observed at, and below, the liquid base of MPCs. The limited range of the MRR
 393 does not appear to introduce a significant bias in the height of the detected cases, as the
 394 median cloud-top (liquid-base) height for MPC events detected by the MRR is 1431 m
 395 (791 m), while that for all cases is 1420 m (826 m). In summary, while the limited range
 396 of the MRR does not affect the height of the detected MPC events, its lower sensitiv-
 397 ity leads to the detection of events that produce higher reflectivities. These events ap-
 398 pear to be characterized by a longer duration, slightly higher LWP values, and colder
 399 cloud-top temperatures.

400 **4.2 Characteristic sizes and fall speeds of precipitating ice particles in**
 401 **the lowest 1 km**

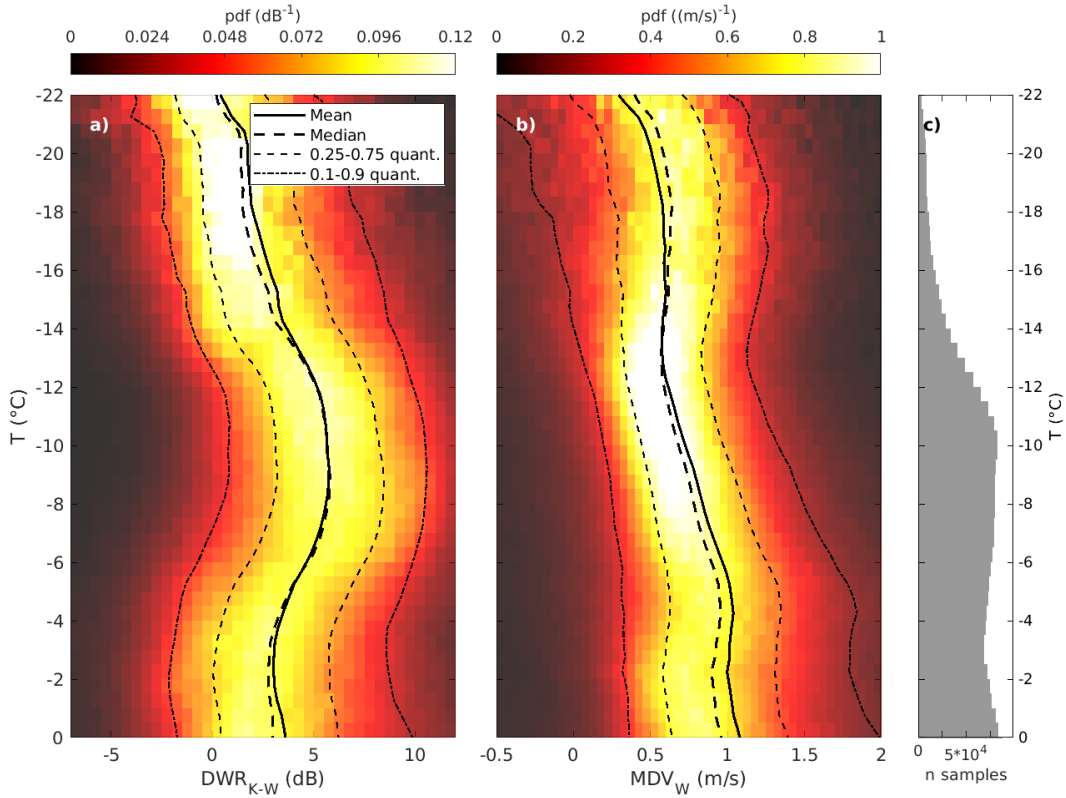


Figure 3. Contoured frequency by temperature diagram (CFTD) of Dual-Wavelength Ratio (DWR; panel a) and Mean Doppler Velocity (MDV; panel b) in the detected mixed-phase cloud events. Panel c displays the number of samples available at each temperature level. MDV values are only included if MRR echoes are available. Bin sizes are: 1 dB, 0.05 m/s, and 0.5 °C.

402 In Fig. 3 we perform long-term statistics of DWR and Mean Doppler Velocity (MDV,
 403 taken from W-band cloud radar) as function of temperature, in the detected shallow MPC
 404 events. This approach is similar to what has been applied to triple-wavelength obser-
 405 vations in mid-latitude clouds by Dias Neto et al. (2019) and Ori et al. (2020). The main
 406 difference in our study is that we focus on shallow MPCs and are restricted to the low-
 407 est 960 m, as well as clouds that produce large enough Z_e signals to be detected by the
 408 MRR. The DWR and MDV statistics in Fig. 3 are displayed as Contoured Frequency
 409 by Temperature Diagrams (CFTDs, Yuter and Houze Jr (1995)). Here, DWR and MDV
 410 values are matched with temperature (T) retrieved at the same height, and the Figure

411 displays joint histograms of DWR and T (panel a), and MDV and T (panel b). These
 412 histograms are normalized to one at each chosen T level. Note that, unlike many other
 413 studies where CFTDs are employed, panels a and b in Fig. 3 should not be interpreted
 414 as continuous profiles. Because of the limited depth of shallow MPCs, and the limited
 415 range of the MRR, each available profile only spans a portion of the displayed temper-
 416 ature range. The mean temperature difference between the lowest W-band cloud radar
 417 range gate (100 m), and the highest MRR range gate (960 m) is 5.2 °C, with 1.8 °C stan-
 418 dard deviation. The total number of samples (Fig. 3c) reveals that 90% (95%) of obser-
 419 vations occur at temperatures higher than -12.7°C (-15.1°C), with maxima at -10 and
 420 0°C.

421 Fig. 3 displays that at temperatures below -15°C median DWR values are close to
 422 1 dB, corresponding to median sizes smaller than 1 mm. Median DWR then rapidly in-
 423 creases to 4.1 dB between -15°C and -12°C. These enhanced DWR signals can be found
 424 at temperatures as high as -6°C, with a distinct maximum between -12 and -8°C (5.6 dB).
 425 At temperatures close to 0°C, the median DWR decreases back to lower values, with a
 426 median of 2.7 dB between -5 and 0°C. Similarly, median MDV in Fig. 3b has a relatively
 427 constant value of 0.6 m/s between -20 and -12°C, typical for small ice crystals (Kajikawa,
 428 1972; Mitchell, 1996; Barthazy & Schefold, 2006; Heymsfield & Westbrook, 2010), grown
 429 most likely by vapor deposition. At the -13°C level where the DWRs increase, we also
 430 find the MDVs to increase. Interestingly, while the DWRs seem to remain almost con-
 431 stant between -12°C and -8°C, the MDVs steadily increase, reaching values close to 1 m/s,
 432 which is a typical terminal velocity of larger aggregates (Locatelli & Hobbs, 1974; Heyms-
 433 field et al., 2007; Brandes et al., 2008; Karrer et al., 2020). A similar behaviour in terms
 434 of both DWR and MDV can be noticed in the case study in Fig. 1 as well. Combining
 435 DWR and MDV information, together with previous knowledge from mid-latitude clouds,
 436 we thus hypothesize that aggregation might play an important role in the formation of
 437 the high-DWR hydrometeors we observe between -15 and -5 °C. The region of increas-
 438 ing DWR starting at -15°C is likely associated with intensified aggregation of branched
 439 dendritic particles growing in the dendritic-growth zone (DGZ). An increase in DWR
 440 associated with enhanced aggregation in the DGZ has been previously observed in mid-
 441 latitude clouds (Dias Neto et al., 2019; Barrett et al., 2019; Ori et al., 2020; Lamer et
 442 al., 2021; Oue et al., 2021). The presence of high-DWR particles at temperatures above
 443 -10°C in Fig. 3a could be simply a result of particles which mainly aggregated in the DGZ
 444 and then sedimented to warmer temperatures, while continuing to aggregate.

445 The low fall velocities observed in Fig. 3a-b at temperatures below -5°C are not
 446 indicative of severe riming that could explain the observed DWRs. However, we cannot
 447 rule out the possibility of light riming of the larger aggregates, as well as smaller rimed
 448 particles as their terminal fall velocities could overlap with the fall velocity of larger, un-
 449 rimed aggregates. Riming has in fact been observed to occur frequently in Arctic MPCs
 450 (McFarquhar et al., 2007; Mioche et al., 2017; Fitch & Garrett, 2022). However, the MDVs
 451 from 72.3% (82.7, 91.6%) of the observed echoes are slower than 1.0 m/s (1.2, 1.5 m/s)
 452 between -15 and -5°C, which corresponds to a rime mass fraction of 0.31 (0.47, 0.65) ac-
 453 cording to Kneifel and Moisseev (2020). It further appears unlikely that the DWR in-
 454 crease at -15°C is mainly driven by riming: first, we are not aware of any evidence that
 455 riming preferentially occurs at -15°C. Second, in this temperature regime the Wegener-
 456 Bergeron-Findeisen process has its maximum (A. V. Korolev & Mazin, 2003) and has
 457 been shown to further hamper formation and survival of liquid droplets (Silber, McG-
 458 lynn, et al., 2021).

459 Although the DWRs at temperatures warmer than -5°C decrease back to lower val-
 460 ues (median of 2.7 dB between -5 and 0°C), the MDVs remain almost constant, close to
 461 1 m/s (median of 1.1 m/s between -5 and 0°C). One potential explanation for this sig-
 462 nature could be the higher terminal fall velocity of columns and needle particles, which
 463 preferentially grow above -10°C by vapor deposition (e.g., Bailey & Hallett, 2009). They

464 can reach terminal velocities close to 1 m/s at smaller sizes compared to plate-like par-
 465 ticles (Kajikawa, 1972; Mitchell, 1996). Also the presence of supercooled drizzle and po-
 466 tential enhanced riming of smaller ice particles with low DWR could explain the observed
 467 behaviour. The likelihood for the formation of drizzle and intensified riming has been
 468 found to strongly increase at temperatures closer to the melting level (Cortinas Jr et al.,
 469 2004; Zhang et al., 2017; Kneifel & Moisseev, 2020). Overall, the DWR-MDV behaviour
 470 found for MPCs at temperatures close to 0°C is significantly different from what is ob-
 471 served at the mid-latitudes. Several studies observed a second and even stronger DWR
 472 increase from -5°C towards the melting level (Chase et al., 2018; Dias Neto et al., 2019;
 473 Tridon et al., 2019; Ori et al., 2020). Interestingly, we are able to find a similar behaviour
 474 also in Ny-Ålesund in cloud systems that are deeper than 2.5 km, as shown in Appendix
 475 B. The lack of aggregation close to the melting level in the detected shallow MPC events
 476 is further explored in the next section.

477 **4.3 Precipitation formation in the mixed-phase layer**

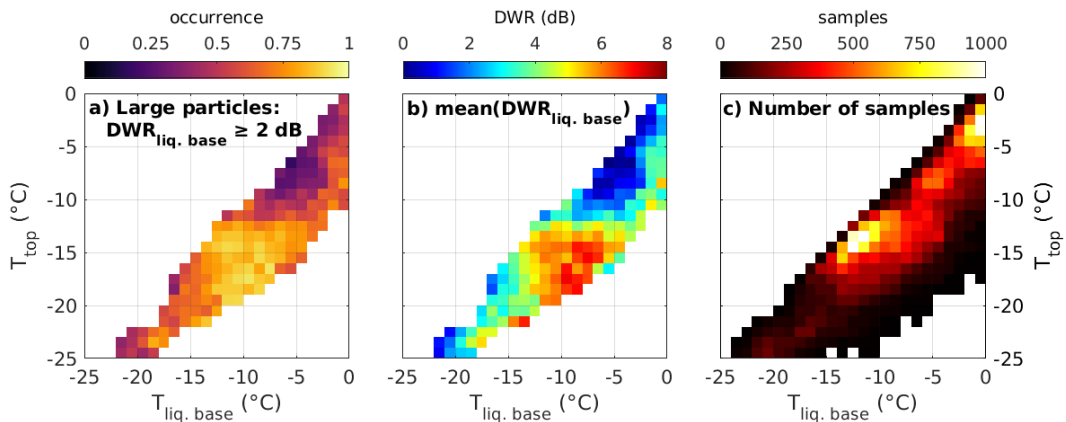


Figure 4. Frequency of occurrence of DWR above 2 dB at liquid base (a), mean DWR at liquid base (b), and number of samples at liquid base (c) as function of cloud-top and liquid-base temperature. In panels a and b bins with less than 60 total samples are ignored. Bins are 1°C wide.

478 In the previous section, we analyzed DWR values with respect to temperature re-
 479 trieved at the same height. We can assume that in shallow MPCs the main nucleation
 480 and initial depositional growth takes place in the mixed-phase layer (MPL), where on
 481 average saturation with respect to liquid water is reached. Therefore, we investigate how
 482 much the particles already aggregate in the MPL and how relevant the temperature of
 483 the MPL is for the occurrence of larger aggregates in the entire profile.

484 We analyze the DWRs observed at the liquid-base height, and relate it to the cloud-
 485 top and liquid-base temperatures in Fig. 4. For a simpler interpretation, in panel a, we
 486 group the profiles into small particles (DWR at liquid base lower than 2 dB, correspond-
 487 ing to a mass median diameter of approximately 1.3 mm; see Fig. A1 in Appendix A)
 488 and larger particles (DWR at liquid base equal or higher than 2 dB), that are most likely
 489 a result of aggregation and/or riming. The threshold of 2 dB was also chosen because
 490 of the estimated uncertainty on DWR of 2.1 dB. DWR values higher than 2 dB can thus
 491 confidently be attributed to non-Rayleigh scattering by hydrometeors. We also tested
 492 slightly different DWR thresholds but did not find a substantial impact on the results
 493 (not shown). Fig. 4a thus shows the frequency of occurrence of DWRs at liquid base higher
 494 than 2 dB. Panels b and c in the Figure display the mean DWR value at liquid base, and

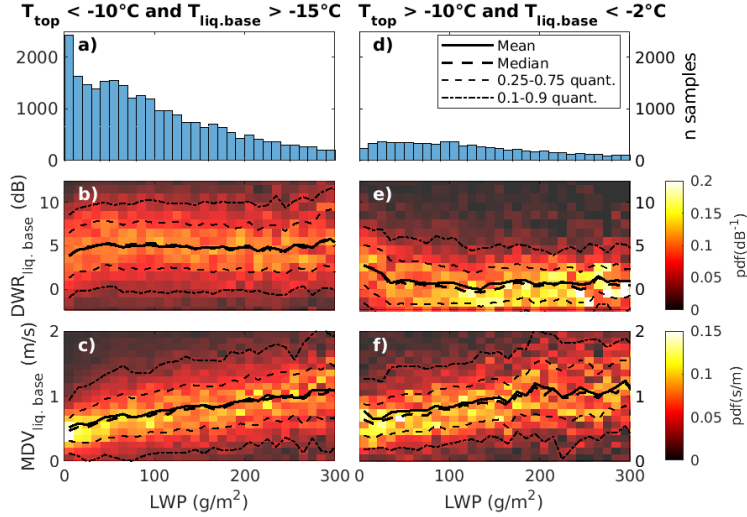


Figure 5. LWP distribution (a, d), and joint DWR-LWP (b, e), and MDV-LWP (c, f) distributions for MPC events in two distinct regimes. Panels a, b and c include MPC events whose mixed-phase layer is at least partly in the temperature interval between -15 and -10°C . Panels d, e and f include MPC events whose mixed-phase layer temperature does not exceed -2°C and does not subceed -10°C . The joint distributions in panels b, c, e and f are normalized to one in each LWP bin. Bin-widths are: 5 g/m^2 , 0.5 dB , and 0.05 m/s .

495 number of available samples, respectively, both as function of liquid-base and cloud-top
 496 temperature.

497 Fig. 4a illustrates that large particles appear to mainly originate from mixed-phase
 498 layers with liquid-base temperature higher than -15°C and cloud-top temperature lower
 499 than -10°C . In this temperature regime 76.8% of the samples in fact produce particles
 500 with DWR of 2 dB or larger. The mean DWR value at liquid base (Fig. 4b) also illus-
 501 trates that even very thin MPLs on average generate particles with DWRs of 5 dB or
 502 higher, if they contain temperatures of -13 to -14°C . Interestingly, this overlaps with the
 503 -15.5 to -13.3°C interval, where the laboratory study by Takahashi (2014) observed the
 504 maximum growth rate of plate-like crystals. As expected, if the MPL is thicker (larger
 505 difference between cloud-top and liquid-base temperature), also the mean DWRs increase,
 506 because of the longer time particles can grow by deposition and subsequent aggregation.

507 Fig. 4b shows that enhanced DWR values can also be found at temperatures out-
 508 side the DGZ. However, the mean DWR and overall frequency of occurrence is gener-
 509 ally much lower than what we observe in the DGZ. Interestingly, for the regions outside
 510 the DGZ the MPL also needs to be deeper (i.e., larger temperature difference between
 511 cloud top and liquid base) in order to produce enhanced DWRs.

512 The dependence of DWR and MDV at liquid base on LWP is shown in Fig. 5, for
 513 two separate temperature regimes. Enhanced aggregation in the -10 to -15°C temper-
 514 ature region appears to occur already at relatively small LWP values. No substantial change
 515 in DWR is found for increasing LWP. This independence can be interpreted as a proof
 516 that the observed DWR signature is mainly caused by aggregation rather than riming
 517 as the latter would be expected to increase with LWP. However, 5c shows that the MDV
 518 observed at the liquid base continuously increases with larger LWP. We suspect, that while
 519 riming is not the main mechanism that increases DWR, it is still contributing to the ob-
 520 served increasing particle fall speeds by increasing ice particle density.

521 The preferential growth of dendrites and the subsequent formation of aggregates
 522 in the DGZ is certainly common knowledge in cloud physics (Pruppacher & Klett, 2012)
 523 although many details of these processes are still not thoroughly understood. We believe
 524 that the signatures found in this study are particularly valuable to better constrain the
 525 process of dendritic growth and subsequent aggregation. Unlike in deeper clouds, no par-
 526 ticles from above enter the DGZ in the shallow MPCs that are the focus of this study.
 527 Instead we can assume that all ice particles are nucleated and grown within the relatively
 528 narrow region of the mixed-phase layer. We can further assume that the particles in the
 529 MPL grow in conditions which are close to liquid water saturation. This allows to com-
 530 pare and relate our results directly to recent laboratory experiments investigating de-
 531 positional growth (Takahashi, 2014) or aggregation (Connolly et al., 2012) in the tem-
 532 perature regime of the DGZ.

533 A number of factors are known to be mainly responsible for the rapid formation
 534 of aggregates in the DGZ. Here, if saturation with respect to liquid is reached, super-
 535 saturation with respect to ice can reach values up to 14%, depending on temperature (Pruppacher
 536 & Klett, 2012), and a maximum of the Wegener-Bergeron-Findeisen (WBF) process is
 537 observed (A. Korolev, 2007). Under these conditions, ice particles grow into dendritic
 538 shape (Bailey & Hallett, 2009; Pruppacher & Klett, 2012), which is connected to enhanced
 539 capacitance (Westbrook et al., 2008; Pruppacher & Klett, 2012) and ventilation coeffi-
 540 cients (Takahashi et al., 1991). All these effects together lead to a maximum in the wa-
 541 ter vapor depositional growth on ice particles in this temperature region (Takahashi, 2014;
 542 Takahashi et al., 1991). As already mentioned, Takahashi (2014) found that the depo-
 543 sitional growth rate is maximized between -15.5 and -13.3°C (see their Fig. 6). After a
 544 growth time of 10 minutes, they observed particles reaching maximum sizes of 1.5-1.8mm
 545 with preferentially stellar, dendritic or fern-like habits. This temperature region coin-
 546 cides with the MPL temperatures where we observed the largest DWRs in Fig.4b.

547 In addition to the very favorable depositional growth conditions, the slower termi-
 548 nal fall velocities of dendrites compared to other shapes with similar mass (e.g., Kajikawa,
 549 1972; Mitchell, 1996) allow them to stay in the supersaturated layer of the cloud for a
 550 longer time compared to other ice habits. For example, a 1 mm dendrite falls at 0.3 m/s
 551 while the same sized column, which grows for example at temperatures higher than -10°C ,
 552 has a terminal velocity of 0.8 m/s (Mitchell, 1996). The rapid depositional growth will
 553 eventually lead to a sufficiently large diversity of terminal velocities and particles sizes
 554 needed for collisions. Moreover, turbulent motions frequently observed in the MPL (e.g.,
 555 Morrison et al., 2012) can be expected to further enhance the likelihood for particle col-
 556 lisions. Their unique shape allows them to stick to each other by mechanical entangle-
 557 ment of their branches (Pruppacher & Klett, 2012; Connolly et al., 2012).

558 The question remains, why do we not observe major DWR increases due to par-
 559 ticle aggregation close to the melting level in shallow MPCs? Fig. 4 highlights that in-
 560 creases in DWR are indeed observed at the liquid base, when its temperature is between
 561 -2 and 0°C . Considering the 2 K uncertainty in the temperature retrievals, we cannot
 562 exclude that this signature is caused by melting particles. Even if melting particles are
 563 not responsible for the enhanced DWRs, the DWRs found close to 0°C in figures 3 and
 564 4 are still significantly smaller than those observed in previous studies for mid-latitude
 565 clouds (Chase et al., 2018; Dias Neto et al., 2019; Tridon et al., 2019; Ori et al., 2020),
 566 and in deeper cloud systems in Ny-Ålesund as well (Appendix B).

567 In general, enhanced aggregation close to the melting level is thought to be caused
 568 by the thickening of a quasi-liquid layer (QLL) on the snowflake surface (Fletcher, 1962;
 569 Fabry & Zawadzki, 1995; Slater & Michaelides, 2019). This QLL forms on any ice par-
 570 ticle, whether being a single crystal, aggregate, or rimed particle, and it increases its ag-
 571 gregation efficiency by enhancing its sticking efficiency. In extreme scenarios, this can
 572 lead to the formation of snowflakes several centimeters in size (Lawson et al., 1998). The
 573 absence of this second enhanced aggregation zone cannot be explained with a lower ice

574 number concentration close to the melting level in shallow MPCs: airborne in-situ mea-
 575 surements have shown similar ice number concentrations for MPCs in cases with cloud-
 576 top temperature (CTT) between -10 and 0 $^{\circ}\text{C}$, compared to cases with CTT between -20
 577 and -10 $^{\circ}\text{C}$ (Rangno & Hobbs, 2001; Mioche et al., 2017). Furthermore, signatures of sec-
 578 ondary ice processes have been observed in Arctic MPCs close to the melting level (Luke
 579 et al., 2021).

580 Although we cannot provide a conclusive answer to this question with our remote
 581 sensing observations alone, we discuss possible processes that could lead to the observed
 582 lack of aggregation. First, the depositional growth rate above -10 $^{\circ}\text{C}$ is at least one or-
 583 der of magnitude smaller than at -15 $^{\circ}\text{C}$ (see e.g. Fig. 4 in Takahashi et al. (1991)). Due
 584 to the higher terminal fall velocities of columns, needles, and isometric particles, which
 585 are often observed in this temperature regime, the time for the particles to grow by de-
 586 position is also much shorter than in the DGZ. A more frequent occurrence of riming,
 587 which was found in Kneifel and Moisseev (2020) to rapidly increase from -12 $^{\circ}\text{C}$ towards
 588 0 $^{\circ}\text{C}$, could further enhance the particles' terminal velocities and limit their residence time
 589 in the MPL. Remote sensing observations of single-layer MPCs above Ny-Ålesund have
 590 in fact shown a liquid fraction above 0.9 in more than 90% (80%) of the cases, when cloud-
 591 top temperature is above -5 $^{\circ}\text{C}$ (between -10 and -5 $^{\circ}\text{C}$) (Nomokonova, Ebell, et al., 2019).
 592 In contrast, liquid fractions for single-layer MPCs with cloud-top temperatures between
 593 -15 and -10 $^{\circ}\text{C}$ is below 0.8 in approximately 50% of the cases (Nomokonova, Ebell, et
 594 al., 2019). The dependence of DWR and MDV on LWP for MPCs in this temperature
 595 regime displayed in Fig. 5e-f is also compatible with increased riming. DWR values are
 596 in fact close to 0 dB for LWP values larger than 15 g/m^2 , and MDV values tend to in-
 597 crease with increasing LWP.

598 4.4 Further aggregation below the mixed-phase layer

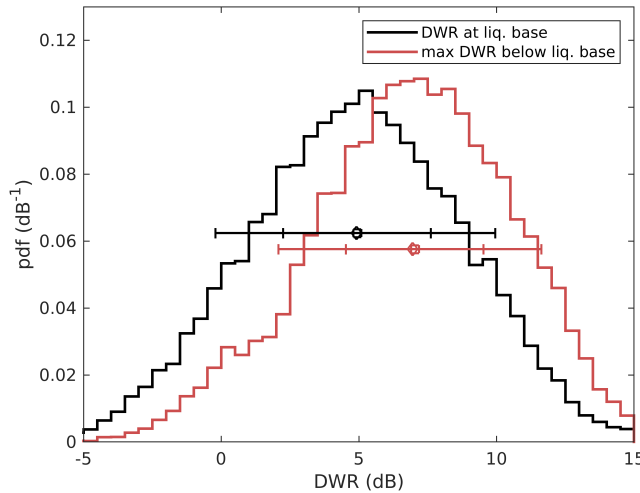


Figure 6. Probability density functions (pdfs) for DWR values at and below the liquid base in shallow MPCs. The black line is relative to values observed at liquid base, while the red line is relative to the maximum DWR value observed in each column below the liquid base. Error bars display 0.1, 0.25, 0.75 and 0.9 quantiles of the two distributions, with diamonds representing the mean values, and squares representing the median values. The data used are only for MPC events with liquid base temperature above -15 $^{\circ}\text{C}$ and cloud-top temperature below -10 $^{\circ}\text{C}$. Samples with surface temperature above 0 $^{\circ}\text{C}$ are excluded. Bins are 0.5 dB wide.

599 While the growth of dendritic branches from ice particles is likely to mostly take
600 place in the mixed-phase layer of the MPC, as it requires high supersaturations with re-
601 spect to ice (Pruppacher & Klett, 2012), aggregation of ice particles can be expected to
602 continue below it. Further increases in DWR below the MPL are in fact observed in the
603 case study shown in Fig. 1, for example on 4 February 2021 between 7 and 11 UTC or
604 between 22 and 24 UTC on the same day. In this section, we evaluate the further DWR
605 increase below the MPL and how strong this increase is in relation to the aggregation
606 signal at the liquid base. We restrict the analysis to profiles where the liquid-base tem-
607 peratures are above -15°C and the cloud-top temperatures are below -10°C as this is the
608 region where we find the majority of large DWR signatures at liquid base. Connecting
609 processes at different heights in one vertical profile is challenging, as the particles are ad-
610 vected by changing horizontal winds causing often complex fall streaks in the radar time-
611 height display (Kalesse, Szyrmer, et al., 2016; Pfitzenmaier et al., 2017, 2018). In order
612 to avoid these difficulties, we do not directly compare DWR values measured at differ-
613 ent heights in the same column. Instead we analyze in Fig. 6 the distributions of DWR
614 values observed at liquid base, and of the maximum DWR values observed below the liq-
615 uid base in each column. Note that in a given column these two values can be the same,
616 if the maximum DWR is at liquid base: this is observed in 15.3% of the available sam-
617 ples. In order to avoid high-DWR signals originating from melting particles, samples mea-
618 sured when surface temperature was above 0°C are ignored in this analysis.

619 From Fig. 6 it is clear that aggregation continues to increase mean aggregate size
620 despite the likely sub-saturated air below liquid base (e.g., Shupe et al., 2008). The me-
621 dian (mean) of the largest DWRs observed below the MPL is 7.0 dB (6.9 dB), and is 43%
622 (41%) larger than the median (mean) DWR of 4.9 dB (4.9 dB) at liquid base. Below the
623 liquid base we can attribute most of the DWR increase to aggregation, as riming can-
624 not occur because of the absence of liquid water. The narrower distribution of the max-
625 imum DWR below liquid base is due to the fact that the DWRs approach the satur-
626 ation value, as the particle sizes grow. DWR saturation values for unrimed and lightly
627 rimed aggregates have been estimated in Appendix A to be 10-11 dB for the 24 and 94
628 GHz combination.

629 4.5 Persistence of high-DWR signals

630 Several previous studies demonstrated that Arctic MPCs display a complex hori-
631 zontal structure, and high spatial variability in terms of dynamics and hydrometeors (Shupe
632 et al., 2008; Schäfer et al., 2018; Eirund et al., 2019; Ruiz-Donoso et al., 2020). It ap-
633 pears therefore interesting to investigate whether the observed high-DWR signatures are
634 restricted to limited regions of the MPC, as observed in Fig. 1, or whether enhanced ag-
635 gregation tends to occur uniformly across the cloud field.

636 The vertically-pointing radars used in this study do not resolve the complete hori-
637 zontal structure of the cloud field but rather observe the variability of clouds that are
638 advected over the measurement site. The observed variability is thus usually a combi-
639 nation of temporal and spatial variability, and spatial variability is only resolved along
640 the wind direction (e.g., Shupe et al., 2008). We estimated the duration of DWR signals
641 exceeding certain thresholds and related them to the total duration of the MPC event
642 (detected by the more sensitive W-band cloud radar, see section 3). The full distribu-
643 tion of this quantity, together with its values for the case study in Fig. 1, is shown in
644 Fig. 7. Note that, unlike the statistics presented in sections 4.2, 4.3 and 4.4, all avail-
645 able samples during MPC events were analyzed, including those with no signal in the
646 MRR data. We'd like to also highlight that the statistics shown in Fig. 7 are sensitive
647 to the definition of MPC event, as this in turn affects the event duration.

648 For interpreting Fig. 7 it might help to consider first the red curve which repre-
649 sents the distribution of DWRs in relation to the event duration from the case shown

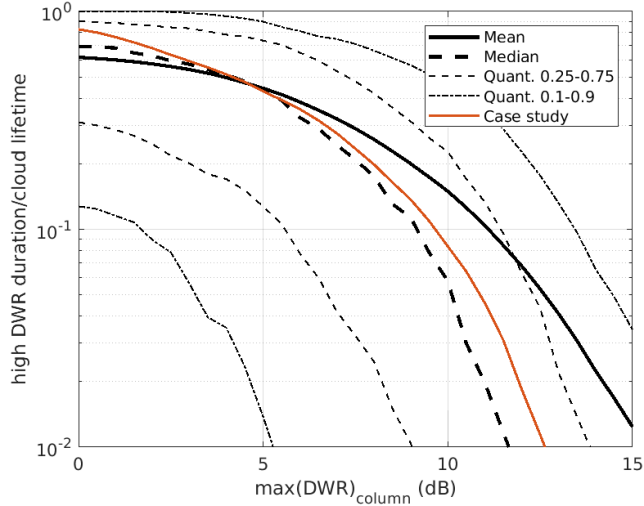


Figure 7. Distributions of the ratio between the duration of high-DWR signals and the total duration of the MPC event. The duration of high-DWR signals is calculated as the total time during an MPC event that the maximum DWR in each column exceeds the value indicated on the x-axis. The curves indicate the mean, median and quantiles of the duration ratio. Only MPC events with the mixed-phase layer at least partly at temperatures between -15 and -10°C are included. The red curve represents the case study observed on 4 to 6 February 2021, illustrated in Fig. 1. Note that the quantity indicated on the y-axis, being a ratio between time intervals, is unitless.

650 in Fig. 1. We see that cloud regions where the maximum DWR in each column exceeds
 651 5 dB appear for 43.1% of the total MPC duration. Higher DWR values, for example ex-
 652 ceeding 8 dB, are only observed for 19.8% of the total duration of the event. The ten-
 653 dency of finding larger DWR values in shorter time periods of the cloud can also be ob-
 654 served when looking at the temporal DWR evolution shown in Fig. 1c. High DWRs in
 655 the case study do not display a straight-forward relation with features in the MDV (e.g.,
 656 upward motions) or the reflectivity field.

657 Similarly to the case study, 50% of all MPC cases (median line) display DWR val-
 658 ues larger than 5 dB for at least 43.8% of the event duration. For larger DWR thresh-
 659 olds, the quantile curves bend relatively quickly to decreasing duration ratios. Again,
 660 this result highlights that high-DWR particles appear to form in limited regions of the
 661 cloud layer and for a limited amount of time, when compared to the cloud overall ex-
 662 tent and duration. In summary, Fig. 7 reveals that 50% of the observed MPCs display
 663 DWR values equal or higher than 2 (5, 8) dB for at least 62.5% (43.8%, 17.5%) of the
 664 total cloud duration. At the same time, 25% of the observed MPCs display DWR val-
 665 ues equal or higher than 2 (5, 8) dB for at least 84.5% (70.2%, 36.1%) of the total cloud
 666 duration.

667 The analysis shown in the previous sections strongly suggests that temperatures
 668 compatible with the DGZ are essential in order for MPCs to produce large aggregates.
 669 However, their occurrence in limited regions of the MPC indicates that temperature might
 670 not be the only driver. Previous studies have shown that dynamical processes are essen-
 671 tial in producing ice precipitation in Arctic MPCs, and that precipitation is in turn in-
 672 tertwined with the organization of the stratocumulus deck (Shupe et al., 2008; Eirund
 673 et al., 2019). At the same time, aerosol concentrations, surface conditions and surface
 674 coupling significantly affect the phase partitioning (Kalesse, de Boer, et al., 2016; Nor-

675 gren et al., 2018; Solomon et al., 2018; Gierens et al., 2020; Griesche et al., 2021). While
 676 we highlighted the relevance of the dendritic-growth zone for the formation of large ag-
 677 gregates in Arctic MPCs, investigating the role of individual processes for the formation
 678 of said aggregates is out of the scope of this study.

679 5 Conclusions and open questions

680 Using a combination of remote sensing instruments, in particular a 24-GHz pre-
 681 cipitation radar and a 94-GHz cloud radar, we evaluated the significance of different ice-
 682 growth processes, with a focus on aggregation, for the formation of precipitation in shal-
 683 low mixed-phase clouds (MPCs) at the high Arctic site of Ny-Ålesund. The combina-
 684 tion of equivalent reflectivity factors measured at two radar frequencies into the Dual-
 685 Wavelength Ratio (DWR) was used to obtain information on the characteristic size of
 686 the particle population. The 3-year statistics of DWR, matched with Mean Doppler Ve-
 687 locity (MDV), thermodynamic retrievals from a microwave radiometer, and phase infor-
 688 mation from the Cloudnet target classification, provided robust observational constraints
 689 for the microphysical processes leading to the formation of precipitation in Arctic shal-
 690 low MPCs.

691 This study revealed the unique role of the dendritic-growth zone (DGZ) for the for-
 692 mation of precipitable ice particles in Arctic shallow MPCs, together with the absence
 693 of enhanced aggregation typically observed close to the melting level in deeper cloud sys-
 694 tems. The main findings of this study are as follows:

- 695 • Enhanced DWR signatures occurred predominantly in shallow MPCs whose mixed-
 696 phase layer was, at least partly, at temperatures between -15 and -10°C . This fea-
 697 ture is compatible with similar signatures observed at the mid-latitudes (Dias Neto
 698 et al., 2019; Barrett et al., 2019). This signature is typically attributed to enhanced
 699 aggregation due to mechanical entanglement of ice particles with dendritic branches,
 700 which preferentially grow in this temperature region (Pruppacher & Klett, 2012).
 701 In particular, the highest DWR values at the liquid base of the MPC were observed
 702 in conjunction with temperatures of -13 to -14°C , in agreement with laboratory
 703 studies that reported the highest depositional-growth rates at these temperatures
 704 (Takahashi et al., 1991; Takahashi, 2014). While riming likely also plays a role,
 705 as confirmed by increasing MDV with LWP, we argue that the growth of the larger
 706 ice particles is to be mainly attributed to rapid depositional growth of plate-like
 707 particles, and subsequent aggregation. Moreover, the relevance of aggregation in
 708 Arctic shallow MPCs in this temperature region is further confirmed by the ad-
 709 ditional increase in DWR observed below the liquid base, where riming cannot take
 710 place.
- 711 • While our results demonstrate that mixed-phase layer temperatures compatible
 712 with dendritic growth are essential for the formation of large aggregates, these larger
 713 hydrometeors are only observed in limited regions of the cloud field. This suggests
 714 that dynamical processes might be at play in the formation of these larger aggre-
 715 gates. We reckon that further investigation is needed to understand the link be-
 716 tween the growth of dendritic particles and their subsequent aggregation, and dy-
 717 namics in Arctic low-level MPCs.
- 718 • Typically a second enhanced aggregation zone close to 0°C is observed in mid-latitude
 719 clouds (Fabry & Zawadzki, 1995; Dias Neto et al., 2019), and in deeper cloud sys-
 720 tems in Ny-Ålesund as well. This is usually attributed to the increased sticking
 721 efficiency of melting ice particles. The lack of high-DWR signals close to the melt-
 722 ing level (-5 to 0°C) in shallow MPCs in Ny-Ålesund suggests that this process
 723 is absent in these clouds. Since shallow MPCs span a limited temperature range,
 724 particles sedimenting from colder temperatures might be necessary to trigger the
 725 enhanced aggregation typically observed. As such, further investigating this tem-

726 perature regime bears the potential to substantially improve our understanding
 727 of aggregation in general, not only limited to shallow MPCs. While we cannot pro-
 728 vide a conclusive answer from the remote-sensing perspective, we speculate that
 729 specific ice habits and increased riming might contribute to the suppression of ag-
 730 gregation. Ice habits that grow above -10°C typically have faster fall velocities and
 731 smaller cross sections than dendrites (Kajikawa, 1972; Mitchell, 1996; Pruppacher
 732 & Klett, 2012). Mean Doppler velocity information, together with evidence of in-
 733 creased drizzle production and riming reported in previous studies (Cortinas Jr
 734 et al., 2004; Zhang et al., 2017; Nomokonova, Ebell, et al., 2019; Kneifel & Moisseev,
 735 2020), indicates that riming might also be relevant at these temperatures, and might
 736 suppress aggregation.

737 While the multi-frequency and Doppler radar observations presented in this study
 738 provided strong observational constraints for the microphysical processes taking place
 739 in Arctic shallow MPCs, the range of observational fingerprints can be substantially ex-
 740 tended with polarimetric observations. The recent extension of the AWIPEV site with
 741 a polarimetric Ka-band radar will allow us to better constrain ice particle concentration
 742 and shape in the future. It will further enable us to obtain DWR profiles reaching cloud
 743 top, as well as overcome the sensitivity limitations of the MRR. In this regard, dual-frequency
 744 cloud radar observations provide the unique opportunity to test and improve the rep-
 745 resentation of ice-growth processes in numerical models (Ori et al., 2020; Karrer et al.,
 746 2021), and this possibility will be in the future explored with the ICOSahedral Non-hydrostatic
 747 (ICON) modelling framework (Zängl et al., 2015), in its Large Eddy Model (LEM) ver-
 748 sion.

749 **Appendix A Examples of DWR dependence on particle size**

750 Fig. A1 illustrates examples of DWR dependence on ice particle shape and size.
 751 DWR values were computed using the scattering database developed by Ori et al. (2021).
 752 Particle size distribution is assumed to be inverse exponential, and the figure shows the
 753 dependency of DWR on the mass median diameter D_0 . The chosen particle types are
 754 unrimed dendrite aggregates, unrimed column and dendrite aggregates, and rimed col-
 755 umn and dendrite aggregates. Three values for the degree of riming have been chosen,
 756 indicated by the Effective LWP (ELWP): 0.1, 0.2 and 0.5 kg/m^2 . ELWP is defined as
 757 the liquid water path that produces the simulated amount of riming, assuming a rim-
 758 ing efficiency of 100 % (Leinonen & Szyrmer, 2015; Leinonen et al., 2018). The Figure
 759 shows that DWR is 0 dB when D_0 is 1 mm for all particle types, it then rapidly increases
 760 as D_0 increases. It then reaches a saturation value between 10 and 11 dB for unrimed
 761 and lightly rimed ($\text{ELWP} = 0.1, 0.2 \text{ kg/m}^2$) aggregates, above 10 mm. The saturation
 762 value is higher for higher degrees of riming.

763 **Appendix B DWR signatures in deep cloud systems in Ny-Ålesund**

764 Similarly to Fig. 3, Fig. B1 displays Contoured Frequency by Temperature diagrams
 765 (CFTDs) of DWR and MDV. Only cloud systems with cloud-top height higher than 2.5
 766 km were selected for this figure. DWR and MDV values are matched with temperature
 767 (T) retrieved at the same height, and the Figure displays joint histograms of DWR and
 768 T (panel a), and MDV and T (panel b).

769 In addition to the typical increase in DWR corresponding to the dendritic-growth
 770 zone (Dias Neto et al., 2019; Barrett et al., 2019; Ori et al., 2020; Lamer et al., 2021; Oue
 771 et al., 2021), the figure displays a further increase of DWR close to the melting level, which
 772 is typically observed at the mid-latitudes (Chase et al., 2018; Dias Neto et al., 2019; Tri-
 773 don et al., 2019; Ori et al., 2020).

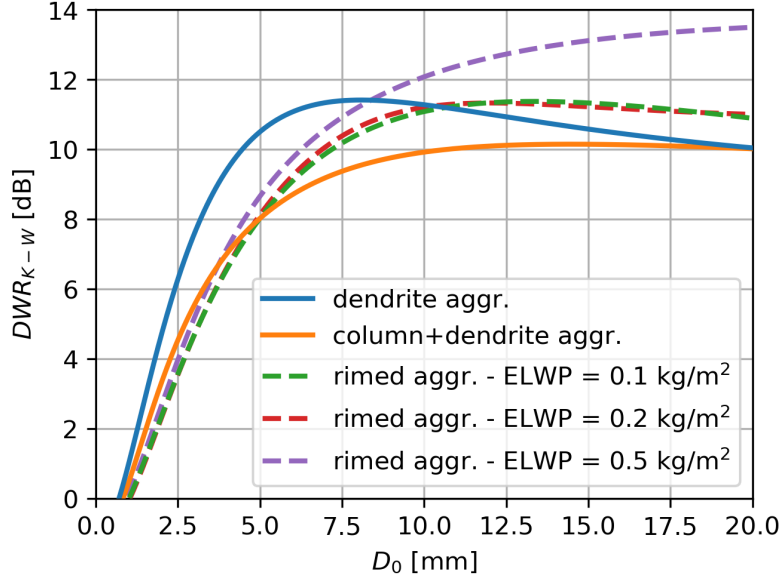


Figure A1. Calculation of DWR at K- (24.2 GHz) and W-band (94.0 GHz) for different ice particle types, as function of the mass median diameter D_0 , obtained with the scattering database by Ori et al. (2021). The ice particles included are: unrimed dendrite aggregates, unrimed dendrite and column aggregates, and rimed dendrite and column aggregates. The degree of riming for the rimed aggregates is indicated by the effective liquid water path (ELWP, see text for definition).

774 **Acknowledgments**

775 We gratefully acknowledge the funding by the Deutsche Forschungsgemeinschaft (DFG,
 776 German Research Foundation) – project no. 268020496 – TRR 172, within the Transre-
 777 gional Collaborative Research Center “Arctic Amplification: Climate Relevant Atmo-
 778 spheric and Surface Processes, and Feedback Mechanisms (AC)3”. Contributions by Ste-
 779 fan Kneifel were funded by the DFG under grant KN 1112/2-1 and KN 1112/2-2 as part
 780 of the Emmy-Noether Group “Optimal combination of Polarimetric and Triple Frequency
 781 radar techniques for Improving Microphysical process understanding of cold clouds” (OP-
 782 TIMIce).

783 This study would not have been possible without Kerstin Ebell and Pavel Krobot,
 784 who managed the data, including the application of the Cloudnet algorithm. In this re-
 785 gard we would also like to thank the Alfred Wegener Institute (AWI) for sharing their
 786 HATPRO and ceilometer data. We wish to thank Lukas Pfitzenmaier, whose assistance
 787 was invaluable when evaluating the calibration of the radar systems, and Davide Ori,
 788 for producing the scattering tables used in the disdrometer-based calibration. We would
 789 like to further acknowledge the discussions with Ulrich Löhnert and Maximilian Maahn,
 790 which helped improve the manuscript. Last but not least, we would like to express our
 791 gratitude to the AWIPEV staff for operating our instruments.

792 GC also acknowledges the support from the Graduate School of Geosciences (GSGS)
 793 of the University of Cologne, as well as the Integrated Research Training Group (IRTG)
 794 of the (AC)3 consortium.

795 **Data availability statement**

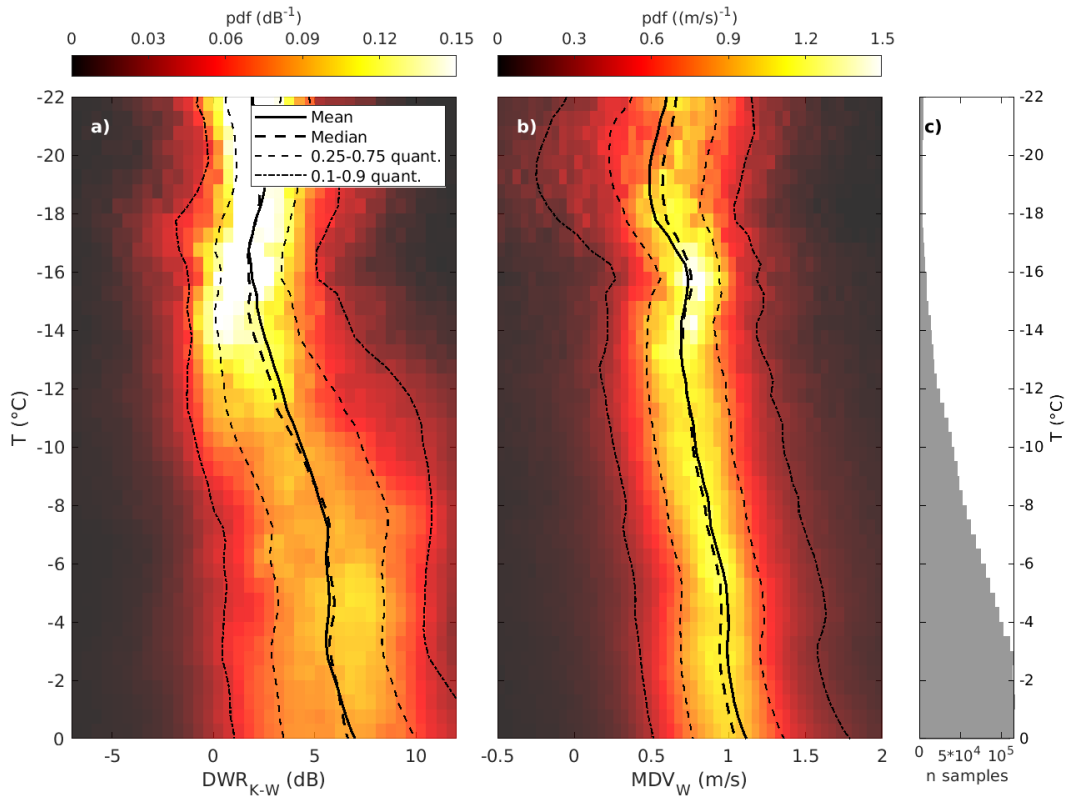


Figure B1. Contoured frequency by temperature diagram (CFTD) of Dual-Wavelength Ratio (DWR) and MDV (Mean Doppler Velocity) in clouds with cloud-top height above 2.5 km. All clouds with cloud-top height above 2.5 km that are detected by the MRR during the study period at sub-zero temperatures are included. Panel c displays the number of samples available at each temperature level. Since MDV is obtained from the W-band cloud radar, MDV values are only included if MRR echoes are available. Bin sizes are: 1 dB, 0.05 m/s, 0.5 °C.

796 Microwave radiometer retrievals for 2017 and 2018 are available in Nomokonova, Ritter,
 797 and Ebell (2019). The Cloudnet target classification product can be downloaded from
 798 <https://cloudnet.fmi.fi/>. The processed DWR and MDV data, and the microwave
 799 radiometer retrievals for 2019, 2020 and 2021 have been submitted to the PANGAEA
 800 archive (<https://pangaea.de>) and will become publicly available during the review pro-
 801 cess. Although not necessary to reproduce the results reported in this study, the MRR
 802 and 94 GHz cloud radar original data will be published in the near future, and will also
 803 be uploaded to the PANGAEA archive.

804 References

- 805 Avramov, A., Ackerman, A. S., Fridlind, A. M., van Dierenhoven, B., Botta, G.,
 806 Aydin, K., ... Wolde, M. (2011). Toward ice formation closure in Arctic
 807 mixed-phase boundary layer clouds during ISDAC. *Journal of Geophysical*
 808 *Research: Atmospheres*, 116(D1). doi: 10.1029/2011JD015910
 809 Avramov, A., & Harrington, J. Y. (2010). Influence of parameterized ice habit on
 810 simulated mixed phase Arctic clouds. *Journal of Geophysical Research: Atmo-*
 811 *spheres*, 115(D3). doi: 10.1029/2009JD012108
 812 Bailey, M. P., & Hallett, J. (2009). A comprehensive habit diagram for atmo-

- spheric ice crystals: Confirmation from the laboratory, AIRS II, and other field studies. *Journal of the Atmospheric Sciences*, 66(9), 2888–2899. doi: 10.1175/2009JAS2883.1
- Barrett, A. I., Westbrook, C. D., Nicol, J. C., & Stein, T. H. M. (2019, May). Rapid ice aggregation process revealed through triple-wavelength Doppler spectrum radar analysis. *Atmospheric Chemistry and Physics*, 19(8), 5753–5769. doi: 10.5194/acp-19-5753-2019
- Barthazy, E., & Schefold, R. (2006). Fall velocity of snowflakes of different riming degree and crystal types. *Atmospheric research*, 82(1-2), 391–398. doi: 10.1016/j.atmosres.2005.12.009
- Battaglia, A., Rustemeier, E., Tokay, A., Blahak, U., & Simmer, C. (2010, February). PARSIVEL Snow Observations: A Critical Assessment. *Journal of Atmospheric and Oceanic Technology*, 27(2), 333–344. doi: 10.1175/2009JTECHA1332.1
- Battaglia, A., Tanelli, S., Tridon, F., Kneifel, S., Leinonen, J., & Kollias, P. (2020). Triple-frequency radar retrievals. In V. Levizzani, C. Kidd, D. B. Kirschbaum, C. D. Kummerow, K. Nakamura, & F. J. Turk (Eds.), *Satellite precipitation measurement: volume 1* (pp. 211–229). Cham: Springer International Publishing. Retrieved from https://doi.org/10.1007/978-3-030-24568-9_13 doi: 10.1007/978-3-030-24568-9_13
- Brandes, E. A., Ikeda, K., Thompson, G., & Schönhuber, M. (2008). Aggregate terminal velocity/temperature relations. *Journal of Applied Meteorology and Climatology*, 47(10), 2729–2736. doi: 10.1175/2008JAMC1869.1
- Cha, J.-W., Chang, K.-H., Yum, S. S., & Choi, Y.-J. (2009). Comparison of the bright band characteristics measured by Micro Rain Radar (MRR) at a mountain and a coastal site in South Korea. *Advances in Atmospheric Sciences*, 26(2), 211–221. doi: 10.1007/s00376-009-0211-0
- Chase, R. J., Finlon, J. A., Borque, P., McFarquhar, G. M., Nesbitt, S. W., Tanelli, S., ... Poellot, M. R. (2018). Evaluation of triple-frequency radar retrieval of snowfall properties using coincident airborne in situ observations during OLYMPEX. *Geophysical Research Letters*, 45(11), 5752–5760. doi: 10.1029/2018GL077997
- Connolly, P., Emersic, C., & Field, P. (2012). A laboratory investigation into the aggregation efficiency of small ice crystals. *Atmospheric Chemistry and Physics*, 12(4), 2055–2076. doi: 10.5194/acp-12-2055-2012
- Cortinas Jr, J. V., Bernstein, B. C., Robbins, C. C., & Walter Strapp, J. (2004). An analysis of freezing rain, freezing drizzle, and ice pellets across the United States and Canada: 1976–90. *Weather and Forecasting*, 19(2), 377–390. doi: [https://doi.org/10.1175/1520-0434\(2004\)019<0377:AAOFRF>2.0.CO;2](https://doi.org/10.1175/1520-0434(2004)019<0377:AAOFRF>2.0.CO;2)
- Crewell, S., & Lohnert, U. (2007). Accuracy of boundary layer temperature profiles retrieved with multifrequency multiangle microwave radiometry. *IEEE Transactions on Geoscience and Remote Sensing*, 45(7), 2195–2201. doi: 10.1109/TGRS.2006.888434
- Dahlke, S., & Maturilli, M. (2017, November). Contribution of Atmospheric Advection to the Amplified Winter Warming in the Arctic North Atlantic Region. *Advances in Meteorology*. doi: 10.1155/2017/4928620
- de Boer, G., Eloranta, E. W., & Shupe, M. D. (2009). Arctic mixed-phase stratiform cloud properties from multiple years of surface-based measurements at two high-latitude locations. *Journal of Atmospheric Sciences*, 66(9), 2874–2887. doi: 10.1175/2009JAS3029.1
- Dias Neto, J., Kneifel, S., Ori, D., Trömel, S., Handwerker, J., Bohn, B., ... Simmer, C. (2019, June). The TRIPLE-frequency and Polarimetric radar Experiment for improving process observations of winter precipitation. *Earth System Science Data*, 11(2), 845–863. doi: 10.5194/essd-11-845-2019
- Durán-Alarcón, C., Boudevillain, B., Genthon, C., Grazioli, J., Souverijns, N., van

- 868 Lipzig, N. P., ... Berne, A. (2019). The vertical structure of precipitation
869 at two stations in East Antarctica derived from micro rain radars. *The*
870 *Cryosphere*, *13*(1), 247–264. doi: 10.5194/tc-13-247-2019
- 871 Ebell, K., Nomokonova, T., Maturilli, M., & Ritter, C. (2020, January). Radiative
872 Effect of Clouds at Ny-Ålesund, Svalbard, as Inferred from Ground-Based Re-
873 mote Sensing Observations. *Journal of Applied Meteorology and Climatology*,
874 *59*(1), 3–22. doi: 10.1175/JAMC-D-19-0080.1
- 875 Eirund, G. K., Lohmann, U., & Possner, A. (2019). Cloud ice processes enhance spa-
876 tial scales of organization in Arctic stratocumulus. *Geophysical Research Let-*
877 *ters*, *46*(23), 14109–14117. doi: 10.1029/2019GL084959
- 878 Fabry, F. (2018). *Radar meteorology: principles and practice*. Cambridge University
879 Press. doi: <https://doi.org/10.1017/CBO9781107707405>
- 880 Fabry, F., & Zawadzki, I. (1995). Long-term radar observations of the melting layer
881 of precipitation and their interpretation. *Journal of Atmospheric Sciences*,
882 *52*(7), 838–851. doi: 10.1175/1520-0469(1995)052<0838:LTROOT>2.0.CO;2
- 883 Fitch, K. E., & Garrett, T. J. (2022). Graupel Precipitating From Thin Arctic
884 Clouds With Liquid Water Paths Less Than 50 g m⁻². *Geophysical Research*
885 *Letters*, *49*(1), e2021GL094075. doi: 10.1029/2021GL094075
- 886 Fletcher, N. H. (1962). Surface structure of water and ice. *Philosophical Magazine*,
887 *7*(74), 255–269. doi: 10.1080/14786436208211860
- 888 Gierens, R. (2021). *Observations of Arctic low-level mixed-phase clouds at Ny-*
889 *Ålesund: Characterization and insights gained by high-resolution Doppler*
890 *radar* (Doctoral dissertation, Universität zu Köln, Köln). Retrieved from
891 <https://kups.ub.uni-koeln.de/53900/>
- 892 Gierens, R., Kneifel, S., Shupe, M. D., Ebell, K., Maturilli, M., & Löhnert, U. (2020,
893 March). Low-level mixed-phase clouds in a complex Arctic environment. *At-*
894 *mospheric Chemistry and Physics*, *20*(6), 3459–3481. doi: 10.5194/acp-20-3459
- 895 -2020
- 896 Grazioli, J., Madeleine, J.-B., Gallée, H., Forbes, R. M., Genthon, C., Krinner, G., &
897 Berne, A. (2017). Katabatic winds diminish precipitation contribution to the
898 Antarctic ice mass balance. *Proceedings of the National Academy of Sciences*,
899 *114*(41), 10858–10863. doi: 10.1073/pnas.1707633114
- 900 Griesche, H. J., Ohneiser, K., Seifert, P., Radenz, M., Engelmann, R., & Ansmann,
901 A. (2021). Contrasting ice formation in arctic clouds: surface-coupled vs.
902 surface-decoupled clouds. *Atmospheric Chemistry and Physics*, *21*(13), 10357–
903 10374. doi: 10.5194/acp-21-10357-2021
- 904 Harrington, J. Y., & Olsson, P. Q. (2001). On the potential influence of ice nuclei on
905 surface-forced marine stratocumulus cloud dynamics. *Journal of Geophysical*
906 *Research: Atmospheres*, *106*(D21), 27473–27484. doi: 10.1029/2000JD000236
- 907 Heymsfield, A. J., Van Zadelhoff, G.-J., Donovan, D. P., Fabry, F., Hogan, R. J., &
908 Illingworth, A. J. (2007). Refinements to ice particle mass dimensional and
909 terminal velocity relationships for ice clouds. Part II: Evaluation and param-
910 eterizations of ensemble ice particle sedimentation velocities. *Journal of the*
911 *atmospheric sciences*, *64*(4), 1068–1088. doi: 10.1175/JAS3900.1
- 912 Heymsfield, A. J., & Westbrook, C. (2010). Advances in the estimation of ice par-
913 ticle fall speeds using laboratory and field measurements. *Journal of the Atmo-*
914 *spheric Sciences*, *67*(8), 2469–2482. doi: 10.1175/2010JAS3379.1
- 915 Hogan, R. J., Illingworth, A. J., & Sauvageot, H. (2000). Measuring crystal size in
916 cirrus using 35- and 94-GHz radars. *Journal of Atmospheric and Oceanic Tech-*
917 *nology*, *17*(1), 27–37. doi: 10.1175/1520-0426(2000)017<0027:MCSICU>2.0.CO;
- 918 2
- 919 Hogan, R. J., & O’Connor, E. J. (2004). Facilitating cloud radar and lidar algo-
920 rithms: the cloudnet instrument synergy/target categorization product. *Cloud-*
921 *net documentation*, *14*.
- 922 Huang, G.-J., Bringi, V. N., & Thurai, M. (2008, September). Orientation Angle

- 923 Distributions of Drops after an 80-m Fall Using a 2D Video Disdrometer. *Journal of Atmospheric and Oceanic Technology*, 25(9), 1717–1723. doi: 10.1175/
924 2008JTECHA1075.1
- 925
- 926 Illingworth, A., Hogan, R., O’connor, E., Bouniol, D., Brooks, M., Delanoë, J., ...
927 others (2007). Cloudnet: Continuous evaluation of cloud profiles in seven
928 operational models using ground-based observations. *Bulletin of the American*
929 *Meteorological Society*, 88(6), 883–898.
- 930 Jackson, R. C., McFarquhar, G. M., Korolev, A. V., Earle, M. E., Liu, P. S., Law-
931 son, R. P., ... Freer, M. (2012). The dependence of ice microphysics on
932 aerosol concentration in arctic mixed-phase stratus clouds during ISDAC and
933 M-PACE. *Journal of Geophysical Research: Atmospheres*, 117(D15). doi:
934 10.1029/2012JD017668
- 935 Kajikawa, M. (1972). Measurement of falling velocity of individual snow crystals.
936 *Journal of the Meteorological Society of Japan. Ser. II*, 50(6), 577–584. doi: 10
937 .2151/jmsj1965.50.6.577
- 938 Kalesse, H., de Boer, G., Solomon, A., Oue, M., Ahlgrimm, M., Zhang, D., ... Pro-
939 tat, A. (2016, December). Understanding Rapid Changes in Phase Parti-
940 tioning between Cloud Liquid and Ice in Stratiform Mixed-Phase Clouds:
941 An Arctic Case Study. *Monthly Weather Review*, 144(12), 4805–4826. doi:
942 10.1175/MWR-D-16-0155.1
- 943 Kalesse, H., Szyrmer, W., Kneifel, S., Kollias, P., & Luke, E. (2016). Fingerprints of
944 a riming event on cloud radar Doppler spectra: observations and modeling. *At-
945 mospheric Chemistry and Physics*, 16(5), 2997–3012. doi: 10.5194/acp-16-2997
946 -2016
- 947 Karrer, M., Seifert, A., Ori, D., & Kneifel, S. (2021). Improving the representation
948 of aggregation in a two-moment microphysical scheme with statistics of multi-
949 frequency Doppler radar observations. *Atmospheric Chemistry and Physics*,
950 21(22), 17133–17166. doi: 10.5194/acp-21-17133-2021
- 951 Karrer, M., Seifert, A., Siewert, C., Ori, D., von Lerber, A., & Kneifel, S. (2020).
952 Ice Particle Properties Inferred From Aggregation Modelling. *Journal*
953 *of Advances in Modeling Earth Systems*, 12(8), e2020MS002066. doi:
954 10.1029/2020MS002066
- 955 Klugmann, D., Heinsohn, K., & Kirtzel, H. J. (1996, February). A low cost 24 GHz
956 FM-CW Doppler radar rain profiler. *Contributions to Atmospheric Physics*,
957 69.
- 958 Kneifel, S., Kollias, P., Battaglia, A., Leinonen, J., Maahn, M., Kalesse, H., & Tri-
959 don, F. (2016, March). First observations of triple-frequency radar Doppler
960 spectra in snowfall: Interpretation and applications. *Geophysical Research*
961 *Letters*, 43(5), 2225–2233. doi: 10.1002/2015GL067618
- 962 Kneifel, S., Maahn, M., Peters, G., & Simmer, C. (2011). Observation of snowfall
963 with a low-power FM-CW K-band radar (Micro Rain Radar). *Meteorology and*
964 *Atmospheric Physics*, 113(1), 75–87. doi: 10.1007/s00703-011-0142-z
- 965 Kneifel, S., & Moisseev, D. (2020). Long-Term Statistics of Riming in Nonconvective
966 Clouds Derived from Ground-Based Doppler Cloud Radar Observations. *Jour-
967 nal of the Atmospheric Sciences*, 77(10), 3495–3508. doi: 10.1175/JAS-D-20
968 -0007.1
- 969 Kobayashi, T. (1957). Experimental researches en the snow crystal habit and growth
970 by means of a diffusion cloud chamber. *Journal of the Meteorological Society of*
971 *Japan. Ser. II*, 35, 38–47. doi: 10.2151/jmsj1923.35A.0.38
- 972 Korolev, A. (2007). Limitations of the Wegener–Bergeron–Findeisen mechanism
973 in the evolution of mixed-phase clouds. *Journal of the Atmospheric Sciences*,
974 64(9), 3372–3375. doi: 10.1175/JAS4035.1
- 975 Korolev, A. V., & Mazin, I. P. (2003). Supersaturation of water vapor in
976 clouds. *Journal of Atmospheric Sciences*, 60(24), 2957–2974. doi:
977 10.1175/1520-0469(2003)060<2957:SOWVIC>2.0.CO;2

- 1032
1031
1030
1029
1028
1027
1026
1025
1024
1023
1022
1021
1020
1019
1018
1017
1016
1015
1014
1013
1012
1011
1010
1009
1008
1007
1006
1005
1004
1003
1002
1001
1000
999
998
997
996
995
994
993
992
991
990
989
988
987
986
985
984
983
982
981
980
979
978
- Küchler, N., Kneifel, S., Löhnert, U., Kollias, P., Czekala, H., & Rose, T. (2017, November). A W-Band Radar–Radiometer System for Accurate and Continuous Monitoring of Clouds and Precipitation. *Journal of Atmospheric and Oceanic Technology*, *34*(11), 2375–2392. doi: 10.1175/JTECH-D-17-0019.1
- Lamer, K., Oue, M., Battaglia, A., Roy, R. J., Cooper, K. B., Dhillon, R., & Kollias, P. (2021). Multifrequency radar observations of clouds and precipitation including the G-band. *Atmospheric Measurement Techniques*, *14*(5), 3615–3629. doi: 10.5194/amt-14-3615-2021
- Lawson, R. P., Stewart, R. E., & Angus, L. J. (1998). Observations and numerical simulations of the origin and development of very large snowflakes. *Journal of the atmospheric sciences*, *55*(21), 3209–3229. doi: 10.1175/1520-0469(1998)055<3209:OANSOT>2.0.CO;2
- Leinonen, J. (2014, January). High-level interface to T-matrix scattering calculations: Architecture, capabilities and limitations. *Optics Express*, *22*(2), 1655–1660. doi: 10.1364/OE.22.001655
- Leinonen, J., Kneifel, S., & Hogan, R. J. (2018). Evaluation of the Rayleigh–Gans approximation for microwave scattering by rimed snowflakes. *Quarterly Journal of the Royal Meteorological Society*, *144*(S1), 77–88. doi: <https://doi.org/10.1002/qj.3093>
- Leinonen, J., & Szyrmer, W. (2015). Radar signatures of snowflake rimming: A modeling study. *Earth and Space Science*, *2*(8), 346–358. doi: 10.1002/2015EA000102
- Liao, L., Meneghini, R., Iguchi, T., & Detwiler, A. (2005). Use of dual-wavelength radar for snow parameter estimates. *Journal of Atmospheric and Oceanic Technology*, *22*(10), 1494–1506. doi: 10.1175/JTECH1808.1
- Locatelli, J. D., & Hobbs, P. V. (1974). Fall speeds and masses of solid precipitation particles. *Journal of Geophysical Research*, *79*(15), 2185–2197. doi: 10.1029/JC079i015p02185
- Löffler-Mang, M., & Joss, J. (2000, February). An Optical Disdrometer for Measuring Size and Velocity of Hydrometeors. *Journal of Atmospheric and Oceanic Technology*, *17*(2), 130–139. doi: 10.1175/1520-0426(2000)017<0130:AODFMS>2.0.CO;2
- Luke, E. P., Yang, F., Kollias, P., Vogelmann, A. M., & Maahn, M. (2021). New insights into ice multiplication using remote-sensing observations of slightly supercooled mixed-phase clouds in the Arctic. *Proceedings of the National Academy of Sciences*, *118*(13). doi: 10.1073/pnas.2021387118
- Maahn, M., Burgard, C., Crewell, S., Gorodetskaya, I. V., Kneifel, S., Lhermitte, S., ... van Lipzig, N. P. (2014). How does the spaceborne radar blind zone affect derived surface snowfall statistics in polar regions? *Journal of Geophysical Research: Atmospheres*, *119*(24), 13–604. doi: 10.1002/2014JD022079
- Maahn, M., & Kollias, P. (2012, November). Improved Micro Rain Radar snow measurements using Doppler spectra post-processing. *Atmospheric Measurement Techniques*, *5*(11), 2661–2673. doi: 10.5194/amt-5-2661-2012
- Mason, S. L., Hogan, R. J., Westbrook, C. D., Kneifel, S., Moisseev, D., & von Terzi, L. (2019, September). The importance of particle size distribution and internal structure for triple-frequency radar retrievals of the morphology of snow. *Atmospheric Measurement Techniques*, *12*(9), 4993–5018. doi: 10.5194/amt-12-4993-2019
- Matrosov, S. Y., Heymsfield, A., & Wang, Z. (2005). Dual-frequency radar ratio of nonspherical atmospheric hydrometeors. *Geophysical research letters*, *32*(13). doi: 10.1029/2005GL023210
- Matrosov, S. Y., Maahn, M., & De Boer, G. (2019). Observational and modeling study of ice hydrometeor radar dual-wavelength ratios. *Journal of Applied Meteorology and Climatology*, *58*(9), 2005–2017. doi: 10.1175/JAMC-D-19-0018.1

- 1033 Maturilli, M., & Ebell, K. (2018, August). Twenty-five years of cloud base height
 1034 measurements by ceilometer in Ny-Ålesund, Svalbard. *Earth System Science*
 1035 *Data*, *10*(3), 1451–1456. doi: 10.5194/essd-10-1451-2018
- 1036 Maturilli, M., Herber, A., & König-Langlo, G. (2013). Climatology and time series
 1037 of surface meteorology in Ny-Ålesund, Svalbard. *Earth System Science Data*,
 1038 *5*(1), 155–163. doi: 10.5194/essd-5-155-2013
- 1039 Maturilli, M., & Kayser, M. (2017). Arctic warming, moisture increase and circula-
 1040 tion changes observed in the Ny-Ålesund homogenized radiosonde record. *The-*
 1041 *oretical and Applied Climatology*, *130*(1), 1–17. doi: 10.1007/s00704-016-1864
 1042 -0
- 1043 Matus, A. V., & L’Ecuyer, T. S. (2017). The role of cloud phase in Earth’s ra-
 1044 diation budget. *Journal of Geophysical Research: Atmospheres*, *122*(5), 2559–
 1045 2578. doi: 10.1002/2016JD025951
- 1046 McFarquhar, G. M., Zhang, G., Poellot, M. R., Kok, G. L., McCoy, R., Tooman,
 1047 T., . . . Heymsfield, A. J. (2007). Ice properties of single-layer stratocumulus
 1048 during the Mixed-Phase Arctic Cloud Experiment: 1. Observations. *Journal of*
 1049 *Geophysical Research: Atmospheres*, *112*(D24). doi: 10.1029/2007JD008633
- 1050 Mech, M., Kliesch, L.-L., Anhäuser, A., Rose, T., Kollias, P., & Crewell, S. (2019,
 1051 September). Microwave Radar/radiometer for Arctic Clouds (MiRAC): First
 1052 insights from the ACLOUD campaign. *Atmospheric Measurement Techniques*,
 1053 *12*(9), 5019–5037. doi: 10.5194/amt-12-5019-2019
- 1054 Mioche, G., Jourdan, O., Ceccaldi, M., & Delanoë, J. (2015). Variability of mixed-
 1055 phase clouds in the Arctic with a focus on the Svalbard region: a study based
 1056 on spaceborne active remote sensing. *Atmos. Chem. Phys.*, *15*(5), 2445–2461.
- 1057 Mioche, G., Jourdan, O., Delanoë, J., Gourbeyre, C., Febvre, G., Dupuy, R., . . .
 1058 Gayet, J.-F. (2017). Vertical distribution of microphysical properties of
 1059 Arctic springtime low-level mixed-phase clouds over the Greenland and Nor-
 1060 wegian seas. *Atmospheric Chemistry and Physics*, *17*(20), 12845–12869. doi:
 1061 10.5194/acp-17-12845-2017
- 1062 Mitchell, D. L. (1996). Use of mass-and area-dimensional power laws for determin-
 1063 ing precipitation particle terminal velocities. *Journal of Atmospheric Sciences*,
 1064 *53*(12), 1710–1723. doi: 10.1175/1520-0469(1996)053<1710:UOMAAD>2.0.CO;
 1065 2
- 1066 Mori, T., Kondo, Y., Ohata, S., Goto-Azuma, K., Fukuda, K., Ogawa-Tsukagawa,
 1067 Y., . . . others (2021). Seasonal Variation of Wet Deposition of Black Carbon
 1068 at Ny-Ålesund, Svalbard. *Journal of Geophysical Research: Atmospheres*, *126*,
 1069 e2020JD034110. doi: 10.1029/2020JD034110
- 1070 Morrison, H., de Boer, G., Feingold, G., Harrington, J., Shupe, M. D., & Sulia, K.
 1071 (2012, January). Resilience of persistent Arctic mixed-phase clouds. *Nature*
 1072 *Geoscience*, *5*(1), 11–17. doi: 10.1038/ngeo1332
- 1073 Myagkov, A., Kneifel, S., & Rose, T. (2020, November). Evaluation of the reflect-
 1074 ivity calibration of W-band radars based on observations in rain. *Atmospheric*
 1075 *Measurement Techniques*, *13*(11), 5799–5825. doi: 10.5194/amt-13-5799-2020
- 1076 Nomokonova, T., Ebell, K., Löhnert, U., Maturilli, M., & Ritter, C. (2020, April).
 1077 The influence of water vapor anomalies on clouds and their radiative effect
 1078 at Ny-Ålesund. *Atmospheric Chemistry and Physics*, *20*(8), 5157–5173. doi:
 1079 10.5194/acp-20-5157-2020
- 1080 Nomokonova, T., Ebell, K., Löhnert, U., Maturilli, M., Ritter, C., & O’Connor,
 1081 E. (2019, April). Statistics on clouds and their relation to thermodynamic
 1082 conditions at Ny-Ålesund using ground-based sensor synergy. *Atmospheric*
 1083 *Chemistry and Physics*, *19*(6), 4105–4126. doi: 10.5194/acp-19-4105-2019
- 1084 Nomokonova, T., Ritter, C., & Ebell, K. (2019). *HATPRO microwave radiometer*
 1085 *measurements at AWIPEV, Ny-Ålesund (2016-2018)* [data set]. PANGAEA.
 1086 Retrieved from <https://doi.org/10.1594/PANGAEA.902183> doi: 10.1594/
 1087 PANGAEA.902183

- 1088 Norgren, M. S., Boer, G. d., & Shupe, M. D. (2018). Observed aerosol suppression of
 1089 cloud ice in low-level Arctic mixed-phase clouds. *Atmospheric Chemistry and*
 1090 *Physics*, *18*(18), 13345–13361. doi: 10.5194/acp-18-13345-2018
- 1091 Ori, D., Schemann, V., Karrer, M., Dias Neto, J., von Terzi, L., Seifert, A., &
 1092 Kneifel, S. (2020). Evaluation of ice particle growth in ICON using statis-
 1093 tics of multi-frequency Doppler cloud radar observations. *Quarterly Journal of*
 1094 *the Royal Meteorological Society*, *146*(733), 3830–3849. doi: 10.1002/qj.3875
- 1095 Ori, D., von Terzi, L., Karrer, M., & Kneifel, S. (2021). snowScatt 1.0: Consis-
 1096 tent model of microphysical and scattering properties of rimed and unrimed
 1097 snowflakes based on the selfsimilar Rayleigh-Gans Approximation. *Geoscientific*
 1098 *Model Development*, *14*(3), 1511–1531. doi: 10.5194/gmd-14-1511-2021
- 1099 Oue, M., Kollias, P., Matrosov, S. Y., Battaglia, A., & Ryzhkov, A. V. (2021). Anal-
 1100 ysis of the microphysical properties of snowfall using scanning polarimetric and
 1101 vertically pointing multi-frequency Doppler radars. *Atmospheric Measurement*
 1102 *Techniques*, *14*(7), 4893–4913. Retrieved from [https://amt.copernicus.org/](https://amt.copernicus.org/articles/14/4893/2021/)
 1103 [articles/14/4893/2021/](https://amt.copernicus.org/articles/14/4893/2021/) doi: 10.5194/amt-14-4893-2021
- 1104 Pfitzenmaier, L., Dufournet, Y., Unal, C. M., & Russchenberg, H. W. (2017). Re-
 1105 trieving fall streaks within cloud systems using Doppler radar. *Journal of*
 1106 *Atmospheric and Oceanic Technology*, *34*(4), 905–920. doi: doi.org/10.1175/
 1107 JTECH-D-16-0117.1
- 1108 Pfitzenmaier, L., Unal, C. M., Dufournet, Y., & Russchenberg, H. W. (2018). Ob-
 1109 serving ice particle growth along fall streaks in mixed-phase clouds using
 1110 spectral polarimetric radar data. *Atmospheric chemistry and physics*, *18*(11),
 1111 7843–7862. doi: 10.5194/acp-18-7843-2018
- 1112 Proske, U., Ferrachat, S., Neubauer, D., Staab, M., & Lohmann, U. (2021). As-
 1113 sessing the potential for simplification in global climate model cloud mi-
 1114 crophysics. *Atmospheric Chemistry and Physics Discussions*, 1–40. doi:
 1115 10.5194/acp-2021-801
- 1116 Pruppacher, H. R., & Klett, J. D. (2012). *Microphysics of clouds and precipitation:*
 1117 *Reprinted 1980*. Dordrecht: Springer. doi: 10.1007/978-94-009-9905-3
- 1118 Rangno, A. L., & Hobbs, P. V. (2001). Ice particles in stratiform clouds in the
 1119 Arctic and possible mechanisms for the production of high ice concentrations.
 1120 *Journal of Geophysical Research: Atmospheres*, *106*(D14), 15065–15075. doi:
 1121 10.1029/2000JD900286
- 1122 Rose, T., Crewell, S., Löhnert, U., & Simmer, C. (2005, May). A network suitable
 1123 microwave radiometer for operational monitoring of the cloudy atmosphere.
 1124 *Atmospheric Research*, *75*(3), 183–200. doi: 10.1016/j.atmosres.2004.12.005
- 1125 Ruiz-Donoso, E., Ehrlich, A., Schäfer, M., Jäkel, E., Schemann, V., Crewell, S., . . .
 1126 others (2020). Small-scale structure of thermodynamic phase in Arctic mixed-
 1127 phase clouds observed by airborne remote sensing during a cold air outbreak
 1128 and a warm air advection event. *Atmospheric Chemistry and Physics*, *20*(9),
 1129 5487–5511. doi: 10.5194/acp-20-5487-2020
- 1130 Sarchilli, C., Ciardini, V., Grigioni, P., Iaccarino, A., De Silvestri, L., Proposito,
 1131 M., . . . Frezzotti, M. (2020). Characterization of snowfall estimated by in
 1132 situ and ground-based remote-sensing observations at Terra Nova Bay, Vic-
 1133 toria Land, Antarctica. *Journal of Glaciology*, *66*(260), 1006–1023. doi:
 1134 10.1017/jog.2020.70
- 1135 Schäfer, M., Loewe, K., Ehrlich, A., Hoose, C., & Wendisch, M. (2018). Simu-
 1136 lated and observed horizontal inhomogeneities of optical thickness of Arctic
 1137 stratus. *Atmospheric Chemistry and Physics*, *18*(17), 13115–13133. doi:
 1138 10.5194/acp-18-13115-2018
- 1139 Serreze, M. C., & Barry, R. G. (2011). Processes and impacts of Arctic amplifica-
 1140 tion: A research synthesis. *Global and planetary change*, *77*(1-2), 85–96. doi:
 1141 10.1016/j.gloplacha.2011.03.004
- 1142 Shupe, M. D. (2011). Clouds at Arctic atmospheric observatories. Part II: Thermo-

- dynamic phase characteristics. *J. Appl. Meteorol. Clim.*, *50*(3), 645–661.
- 1143 Shupe, M. D., & Intrieri, J. M. (2004). Cloud radiative forcing of the Arctic surface:
1144 The influence of cloud properties, surface albedo, and solar zenith angle. *J.*
1145 *Climate*, *17*(3), 616–628.
- 1146 Shupe, M. D., Kollias, P., Persson, P. O. G., & McFarquhar, G. M. (2008). Vertical
1147 motions in Arctic mixed-phase stratiform clouds. *Journal of Atmospheric Sci-*
1148 *ences*, *65*(4), 1304–1322. doi: 10.1175/2007JAS2479.1
- 1149 Shupe, M. D., Matrosov, S. Y., & Uttal, T. (2006a). Arctic mixed-phase cloud
1150 properties derived from surface-based sensors at SHEBA. *Journal of the atmo-*
1151 *spheric sciences*, *63*(2), 697–711. doi: 10.1175/JAS3659.1
- 1152 Shupe, M. D., Matrosov, S. Y., & Uttal, T. (2006b, February). Arctic Mixed-Phase
1153 Cloud Properties Derived from Surface-Based Sensors at SHEBA. *Journal of*
1154 *the Atmospheric Sciences*, *63*(2), 697–711. doi: 10.1175/JAS3659.1
- 1155 Silber, I., Fridlind, A. M., Verlinde, J., Ackerman, A. S., Cesana, G. V., & Knopf,
1156 D. A. (2021). The prevalence of precipitation from polar supercooled
1157 clouds. *Atmospheric Chemistry and Physics*, *21*(5), 3949–3971. doi:
1158 10.5194/acp-21-3949-2021
- 1159 Silber, I., McGlynn, P. S., Harrington, J. Y., & Verlinde, J. (2021). Habit-
1160 Dependent Vapor Growth Modulates Arctic Supercooled Water Occur-
1161 rence. *Geophysical Research Letters*, *48*(10), e2021GL092767. doi:
1162 10.1029/2021GL092767
- 1163 Simpfendorfer, L. F., Verlinde, J., Harrington, J. Y., Shupe, M. D., Chen, Y.-S.,
1164 Clothiaux, E. E., & Golaz, J.-C. (2019). Formation of Arctic stratocumuli
1165 through atmospheric radiative cooling. *Journal of Geophysical Research:*
1166 *Atmospheres*, *124*(16), 9644–9664. doi: 10.1029/2018JD030189
- 1167 Slater, B., & Michaelides, A. (2019). Surface premelting of water ice. *Nature Re-*
1168 *views Chemistry*, *3*(3), 172–188. doi: 10.1038/s41570-019-0080-8
- 1169 Solomon, A., Boer, G. d., Creamean, J. M., McComiskey, A., Shupe, M. D., Maahn,
1170 M., & Cox, C. (2018). The relative impact of cloud condensation nuclei and
1171 ice nucleating particle concentrations on phase partitioning in Arctic mixed-
1172 phase stratocumulus clouds. *Atmospheric Chemistry and Physics*, *18*(23),
1173 17047–17059. doi: 10.5194/acp-18-17047-2018
- 1174 Solomon, A., Feingold, G., & Shupe, M. D. (2015). The role of ice nuclei recy-
1175 cling in the maintenance of cloud ice in Arctic mixed-phase stratocumu-
1176 lus. *Atmospheric Chemistry and Physics*, *15*(18), 10631–10643. Retrieved
1177 from <https://acp.copernicus.org/articles/15/10631/2015/> doi:
1178 10.5194/acp-15-10631-2015
- 1179 Solomon, A., Shupe, M. D., Persson, O., Morrison, H., Yamaguchi, T., Caldwell,
1180 P. M., & de Boer, G. (2014). The sensitivity of springtime Arctic mixed-phase
1181 stratocumulus clouds to surface-layer and cloud-top inversion-layer moisture
1182 sources. *J. Atmos. Sci.*, *71*(2), 574–595.
- 1183 Solomon, A., Shupe, M. D., Persson, P. O. G., & Morrison, H. (2011, Octo-
1184 ber). Moisture and dynamical interactions maintaining decoupled Arctic
1185 mixed-phase stratocumulus in the presence of a humidity inversion. *At-*
1186 *mospheric Chemistry and Physics*, *11*(19), 10127–10148. doi: 10.5194/
1187 acp-11-10127-2011
- 1188 Sotiropoulou, G., Sedlar, J., Tjernström, M., Shupe, M. D., Brooks, I. M., & Pers-
1189 son, P. O. G. (2014). The thermodynamic structure of summer arctic stratocu-
1190 mulus and the dynamic coupling to the surface. *Atmospheric Chemistry and*
1191 *Physics*, *14*(22), 12573–12592. doi: 10.5194/acp-14-12573-2014
- 1192 Souverijns, N., Gossart, A., Lhermitte, S., Gorodetskaya, I. V., Grazioli, J., Berne,
1193 A., . . . van Lipzig, N. P. M. (2018). Evaluation of the CloudSat surface snow-
1194 fall product over Antarctica using ground-based precipitation radars. *The*
1195 *Cryosphere*, *12*(12), 3775–3789. doi: 10.5194/tc-12-3775-2018
- 1196 Szyrmer, W., & Zawadzki, I. (2014). Snow studies. Part IV: Ensemble retrieval of
1197

- 1198 snow microphysics from dual-wavelength vertically pointing radars. *Journal of*
 1199 *the Atmospheric Sciences*, *71*(3), 1171–1186. doi: 10.1175/JAS-D-12-0286.1
- 1200 Takahashi, T. (2014). Influence of liquid water content and temperature on the form
 1201 and growth of branched planar snow crystals in a cloud. *Journal of the Atmo-*
 1202 *spheric Sciences*, *71*(11), 4127–4142. doi: 10.1175/JAS-D-14-0043.1
- 1203 Takahashi, T., Endoh, T., Wakahama, G., & Fukuta, N. (1991). Vapor diffusional
 1204 growth of free-falling snow crystals between -3 and -23°C. *Journal of the Mete-*
 1205 *orological Society of Japan. Ser. II*, *69*(1), 15–30. doi: 10.2151/jmsj1965.69.1
 1206 _15
- 1207 Tan, I., & Storelvmo, T. (2019). Evidence of strong contributions from mixed-
 1208 phase clouds to Arctic climate change. *Geophysical Research Letters*, *46*(5),
 1209 2894–2902. doi: 10.1029/2018GL081871
- 1210 Thurai, M., Huang, G. J., Bringi, V. N., Randeu, W. L., & Schönhuber, M. (2007,
 1211 June). Drop Shapes, Model Comparisons, and Calculations of Polarimetric
 1212 Radar Parameters in Rain. *Journal of Atmospheric and Oceanic Technology*,
 1213 *24*(6), 1019–1032. doi: 10.1175/JTECH2051.1
- 1214 Tridon, F., & Battaglia, A. (2015). Dual-frequency radar Doppler spectral re-
 1215 trieval of rain drop size distributions and entangled dynamics variables.
 1216 *Journal of Geophysical Research: Atmospheres*, *120*(11), 5585–5601. doi:
 1217 10.1002/2014JD023023
- 1218 Tridon, F., Battaglia, A., Chase, R. J., Turk, F. J., Leinonen, J., Kneifel, S., ... oth-
 1219 ers (2019). The microphysics of stratiform precipitation during OLYMPEX:
 1220 Compatibility between triple-frequency radar and airborne in situ observa-
 1221 tions. *Journal of Geophysical Research: Atmospheres*, *124*(15), 8764–8792. doi:
 1222 10.1029/2018JD029858
- 1223 Tridon, F., Battaglia, A., & Kneifel, S. (2020). Estimating total attenuation us-
 1224 ing rayleigh targets at cloud top: applications in multilayer and mixed-phase
 1225 clouds observed by ground-based multifrequency radars. *Atmospheric Measure-*
 1226 *ment Techniques*, *13*(9), 5065–5085. doi: 10.5194/amt-13-5065-2020
- 1227 Vassel, M., Ickes, L., Maturilli, M., & Hoose, C. (2019). Classification of Arctic
 1228 multilayer clouds using radiosonde and radar data in Svalbard. *Atmospheric*
 1229 *Chemistry and Physics*, *19*(7), 5111–5126. doi: 10.5194/acp-19-5111-2019
- 1230 Waterman, P. (1965). Matrix formulation of electromagnetic scattering. *Proceedings*
 1231 *of the IEEE*, *53*(8), 805–812. doi: 10.1109/PROC.1965.4058
- 1232 Wendisch, M., Macke, A., Ehrlich, A., Lüpkes, C., Mech, M., Chechin, D., ... Zep-
 1233 penfeld, S. (2019). The Arctic Cloud Puzzle: Using ACLOUD/PASCAL Mul-
 1234 tiplatform Observations to Unravel the Role of Clouds and Aerosol Particles in
 1235 Arctic Amplification. *Bulletin of the American Meteorological Society*, *100*(5),
 1236 841–871. Retrieved from <https://doi.org/10.1175/BAMS-D-18-0072.1> doi:
 1237 10.1175/BAMS-D-18-0072.1
- 1238 Westbrook, C. D., Hogan, R. J., & Illingworth, A. J. (2008). The capacitance of
 1239 pristine ice crystals and aggregate snowflakes. *Journal of the atmospheric sci-*
 1240 *ences*, *65*(1), 206–219.
- 1241 Williams, C. R., Gage, K. S., Clark, W., & Kucera, P. (2005). Monitoring the
 1242 reflectivity calibration of a scanning radar using a profiling radar and a dis-
 1243 drometer. *Journal of Atmospheric and Oceanic Technology*, *22*(7), 1004–1018.
 1244 doi: <https://doi.org/10.1175/JTECH1759.1>
- 1245 Young, G., Jones, H. M., Choulaton, T. W., Crosier, J., Bower, K. N., Gal-
 1246 lagher, M. W., ... Flynn, M. J. (2016, November). Observed microphysi-
 1247 cal changes in Arctic mixed-phase clouds when transitioning from sea ice to
 1248 open ocean. *Atmospheric Chemistry and Physics*, *16*(21), 13945–13967. doi:
 1249 10.5194/acp-16-13945-2016
- 1250 Yuter, S. E., & Houze Jr, R. A. (1995). Three-dimensional kinematic and mi-
 1251 crophysical evolution of Florida cumulonimbus. Part II: Frequency distribu-
 1252 tions of vertical velocity, reflectivity, and differential reflectivity. *Monthly*

- 1253 *weather review*, 123(7), 1941–1963. doi: 10.1175/1520-0493(1995)123<1941:
1254 TDKAME>2.0.CO;2
- 1255 Zängl, G., Reinert, D., Rípodas, P., & Baldauf, M. (2015). The ICON (ICOsahedral
1256 Non-hydrostatic) modelling framework of DWD and MPI-M: Description of
1257 the non-hydrostatic dynamical core. *Quarterly Journal of the Royal Meteorological Society*, 141(687), 563–579. doi: 10.1002/qj.2378
- 1258 Zhang, D., Wang, Z., Luo, T., Yin, Y., & Flynn, C. (2017). The occurrence of
1259 ice production in slightly supercooled Arctic stratiform clouds as observed by
1260 ground-based remote sensors at the ARM NSA site. *Journal of Geophysical Research: Atmospheres*, 122(5), 2867–2877. doi: 10.1002/2016JD026226
- 1261 Zhao, M., & Wang, Z. (2010). Comparison of Arctic clouds between European
1262 Center for Medium-Range Weather Forecasts simulations and Atmospheric
1263 Radiation Measurement Climate Research Facility long-term observations
1264 at the North Slope of Alaska Barrow site. *Journal of Geophysical Research: Atmospheres*, 115(D23). doi: 10.1029/2010JD014285
- 1265 Zuidema, P., Baker, B., Han, Y., Intrieri, J., Key, J., Lawson, P., . . . Uttal, T.
1266 (2005). An Arctic springtime mixed-phase cloudy boundary layer observed
1267 during SHEBA. *Journal of the atmospheric sciences*, 62(1), 160–176. doi:
1268 10.1175/JAS-3368.1
1271